



**HAL**  
open science

## Soft chemistry synthesis and laser powder bed fusion processing of Fe–Ni alloy based powders

Valérie Baco-Carles, Vincent Baylac, Isabelle Pasquet, Baptiste Plissonneau, Philippe Tailhades

► **To cite this version:**

Valérie Baco-Carles, Vincent Baylac, Isabelle Pasquet, Baptiste Plissonneau, Philippe Tailhades. Soft chemistry synthesis and laser powder bed fusion processing of Fe–Ni alloy based powders: A route for the manufacturing of porous multiphase Fe–Ni alloy parts. *Powder Technology*, 2022, 399, pp.117200. 10.1016/j.powtec.2022.117200 . hal-03819805

**HAL Id: hal-03819805**

**<https://hal.science/hal-03819805>**

Submitted on 19 Oct 2022

**HAL** is a multi-disciplinary open access archive for the deposit and dissemination of scientific research documents, whether they are published or not. The documents may come from teaching and research institutions in France or abroad, or from public or private research centers.

L'archive ouverte pluridisciplinaire **HAL**, est destinée au dépôt et à la diffusion de documents scientifiques de niveau recherche, publiés ou non, émanant des établissements d'enseignement et de recherche français ou étrangers, des laboratoires publics ou privés.

**Soft chemistry synthesis and laser powder bed fusion processing of Fe-Ni alloy based powders: a route for the manufacturing of porous multiphase Fe-Ni alloy parts.**

Valérie Baco-Carles<sup>a\*</sup>, Vincent Baylac<sup>a</sup>, Isabelle Pasquet<sup>a</sup>, Baptiste Plissonneau<sup>a,1</sup>,  
Philippe Tailhades<sup>a</sup>

<sup>a</sup> CIRIMAT, Institut Carnot Chimie Balard CIRIMAT, CNRS-INP-UPS, Université Toulouse 3 Paul Sabatier, 118 Route de Narbonne, F-31062 Toulouse cedex 9, France

\* Corresponding author. Tel.: +33 05 61 55 61 40,

E-mail address: [valerie.baco@univ-tlse3.fr](mailto:valerie.baco@univ-tlse3.fr) (V. Baco-Carles)

Other authors: [vincent.baylac@univ-tlse3.fr](mailto:vincent.baylac@univ-tlse3.fr) (V. Baylac), [isabelle.pasquet@univ-tlse3.fr](mailto:isabelle.pasquet@univ-tlse3.fr)

(I. Pasquet), [plissonneau.baptiste@gmail.com](mailto:plissonneau.baptiste@gmail.com) (B. Plissonneau),

[philippe.tailhades@univ-tlse3.fr](mailto:philippe.tailhades@univ-tlse3.fr) (Ph. Tailhades)

**Abstract**

Fe-Ni alloy based powders of different stoichiometry and purity were synthesized by thermal decomposition of a co-precipitated oxalic precursor. By modifying the oxygen partial pressure of the gaseous flow, a nearly pure Fe<sub>64</sub>Ni<sub>36</sub> Invar powder and a composite Fe<sub>50</sub>Ni<sub>50</sub>-Fe<sub>3</sub>O<sub>4</sub> powder were prepared. The composite particles present an original microstructure consisting of an intimate mixture of Fe<sub>50</sub>Ni<sub>50</sub> and Fe<sub>3</sub>O<sub>4</sub> submicronic grains. The behavior of the composite powder was studied in laser powder bed fusion (LPBF) process. Reduction of iron oxide and specific microstructural changes were revealed. Subsequent conventional heat post-treatment allowed to remove the remaining iron oxides and to form porous multiphase Fe-Ni alloy 3D parts. Repeatable heterogeneities of microstructure and composition, at a periodicity

<sup>1</sup> Baptiste Plissonneau, Speerstrasse 31 Horgen 8810 Switzerland

corresponding to the thickness of the powder bed used in the LPBF process, constitute the hallmark of the laser treatment carried out on the composite powder.

### **Key words**

Metal oxalate; Invar powder; Metal-oxide composite powder; Laser powder bed fusion; Specific microstructure; Porous multiphase Fe-Ni alloy parts.

### **1. Introduction**

Fe-Ni alloys are attractive materials due in particular to their magnetic performances and their extraordinary thermal expansion properties (alloys with no or controlled expansion). As soft magnetic materials with high permeability, low coercivity and low magnetostriction, Fe-Ni alloys and especially permalloys, are largely studied in magnetic materials research field [1-3] and widely applied in industry of magnetic devices, such as sensors, transformers, inductive devices and electric motors [4-8]. Moreover, Invar Fe<sub>64</sub>Ni<sub>36</sub> alloy (Invar36) display very low coefficients of thermal expansion below its Curie point located around 280°C (CTE  $\leq 2 \cdot 10^{-6} \cdot \text{K}^{-1}$  from 20 to 100°C). This phenomenon, known as Invar effect, is extended to other Fe-Ni alloys but also to Fe<sub>72</sub>Pt<sub>28</sub>, FePd<sub>3</sub>... Because of its uniquely low thermal expansion properties [9], Invar36 is ideal for applications where high-dimensional stability is required over a wide range of temperatures (space cameras, precision instruments/tooling, clocks, seismic creep gauges, valves in motors, liquefied natural gas storage tank, antimagnetic watches, optical mounting, metrology devices, time-keeping...) [10].

However, the machining performance of bulk Invar and other austenitic Fe-Ni alloys is relatively poor. These alloys are difficult to cut owing to high work hardening, high ductility and low heat conductivity. Thus, additive manufacturing (AM) is an interesting shaping method for these alloys [11]. Laser powder bed fusion (LPBF), also known as

selective laser melting (SLM) or laser beam melting (LBM) [12-13], is an attractive AM process to fabricate complex shaped metal 3D parts by solidifying a molten metal from a laser source. According to such a process, thin layers of powder are successively spread on a build plate. Each powder bed is melted according to an appropriate laser parameters programming, and merged with the previous consolidated bed to lead to the desired 3D part. Due to its ability to manufacture free-form geometries directly from computer-aided design (CAD) models, LPBF is considered as one of the best technologies for manufacturing complex shaped metal 3D parts, especially for metals that are difficult to machine. In addition, residual stresses, due to large temperature gradients induced by the LPBF process, can be reduced to some extent by using a low CTE material such as Invar36 [14].

The literature reports many works on AM of metallic 3D parts including aluminum and titanium alloys, steels [12, 15] and in a lesser extent, Fe-Ni alloys. Fe-Ni alloys parts were AM processed by Laser Melting Deposition (LMD) [16, 17] or, most frequently, by LPBF [11, 13, 18-25]. The LPBF studies deal with the influence of the modification of the laser parameters (power, scanning velocity and strategy, hatch spacing) on the evolution of the microstructure [19, 21-22], the CTE values [13, 23-24], the magnetic [15, 17-20] and mechanical properties [11, 21, 25] of the Fe-Ni parts. Depending on the lasing conditions, Fe-Ni alloys keep their fcc or bcc crystallographic structure [13, 20] or evolve towards the formation of precipitates with a crystallographic structure different from that of the starting alloy (bcc Fe-Ni precipitates in a fcc Fe-Ni matrix or the reverse) [18-19, 21]. The saturation magnetization of the AM processed Fe-Ni alloys is either equal or higher to the corresponding alloys prepared by conventional methods. The change of coercivity and magnetization is attributed to change of grain

size associated with internal stresses and modification of the Fe-Ni alloys structure (fcc/bcc Fe-Ni phase's ratio) [15, 18-19]. Harrison et al. [23] have revealed that the LPBF process does not affect the low thermal expansion properties of Invar in a negative way. They observed a decrease in the CTE values which can be explained by residual stresses. On the contrary, other authors [13, 24] revealed that LPBF manufactured Invar alloys exhibit CTE values comparable to that of conventional methods. Asgari et al. [13] have shown that an increase in laser power induces texturing along the  $\langle 110 \rangle$  direction parallel to the building axis and consequently an increase in thermal expansion.

Fe-Ni alloy powders can be synthesized by chemical processes involving thermal decomposition of metal precursors. Thus, Cortez et al. [26] have prepared Fe-Ni alloys from thermal decomposition at 400°C of metallic nitrates followed by reduction at 700°C under  $H_2$  of the mixture of the resulting NiO and  $Fe_2O_3$  oxides. Gao et al. [27] have obtained metallic Fe-Ni powders from thermal decomposition at 600°C of mixed hydroxide precursors. Fe-Ni alloys powders are also produced by gas atomization [13, 21, 23-25]. The synthesis of Fe-Ni alloys powders by thermal decomposition of co-precipitated precursors differs from atomization processes by the temperatures involved. Indeed, the soft chemistry route allows obtaining Fe-Ni alloys powders at low temperature ( $T < 600^\circ C$ ), contrary to atomization processes which requires melting Fe-Ni alloys ( $T > 1400^\circ C$ ). Moreover, the co-precipitation method gives rise to a homogeneous combination of nickel and iron cations at the molecular scale within the crystal structure of the mixed precursor. During its thermal decomposition, the prior association of the metallic elements at the molecular scale facilitates the synthesis of Fe-Ni alloy particles of homogeneous composition. In the atomization processes, the

homogeneity of composition of the metal alloy particles is closely dependent on that of the starting metal rods. On the other hand, phase separations can occur during the atomization and solidification steps. Indeed, Qiu et al [21] have revealed the presence of iron-rich bcc Fe-Ni alloy precipitates within each fcc Invar alloy particle obtained by gas atomization. Metal powders issued from atomization processes are however generally used in LPBF process because the particle size (about 15-50  $\mu\text{m}$ ) and the morphological characteristics (spherical particles with smooth surface) of the particles are adequate to allow a good spreading of the metal powder. Fe-Ni alloy 3D parts were manufactured by direct melting of Fe-Ni alloy powders with the desired composition [13, 21, 23-25] or by reactive melting of a mixture of iron and nickel powders in the desired weight ratio [18-20]. We propose in this work to study Fe-Ni alloy based powders synthesized by a soft chemistry route. The process is based on the thermal decomposition under a weakly hydrogenated atmosphere of a metal oxalate precursor. The control of the stoichiometry and the purity of the Fe-Ni alloy obtained are the subject of the first two parts of this work. The behavior in LPBF process of a Fe-Ni/Fe<sub>3</sub>O<sub>4</sub> composite powder, under a weakly hydrogenated atmosphere, was studied in the last part. The influence of the laser processing on the change in nature of the iron oxide phase was first revealed and was followed by a study of thermal post-treatments in order to remove the remaining iron oxides. Porous composites Fe-Ni alloy/iron oxides parts were issued from the LPBF process. Such composite materials are different from those prepared in the literature by laser processing. Li et al. [14] have studied the development of laser deposited Invar-TiC composites for the production of high quality of prototypes for molding and tooling which need low CTE brought by Invar, and high yield strength, good toughness and high wear resistance brought by TiC addition in the

Invar matrix. Microstructure and tensile behavior of LPBF manufactured SiC-Fe composite parts have been studied [28]. S. Dadbakhsh et al. [29, 30] have used in LPBF process, mixtures of Al and Fe<sub>2</sub>O<sub>3</sub> powders with different oxide contents (5 to 15 wt. %), for the production of particles reinforced Al matrix parts. They have revealed that in situ reactions between Al and Fe<sub>2</sub>O<sub>3</sub> powders give rise to the formation in an Al matrix, of secondary phases constituted of Al-Fe intermetallic and Al<sub>2</sub>O<sub>3</sub> oxides with different crystallographic structures. This reaction released extra heat and energy to promote fusion and improved the additive manufacturing over a wide range of laser parameters. Finally, Pasquet et al. [31] have prepared by LPBF process, cermet materials from a mixture of commercial Cu metal powder and Ni<sub>x</sub>Co<sub>y</sub>Fe<sub>3-x-y</sub>O<sub>4</sub> oxide powder synthesized by a soft chemistry route. They obtained a nanostructuring of the initial microstructure, not observed from conventional synthesis method. Despite a high porosity rate, these nanomaterials have revealed potential applications as inert anodes for the electrolysis of aluminum. Due to their originality, the LPBF processed parts, raw and thermally post-treated, manufactured in this work were also characterized in this paper.

## **2. Experimental**

### *2.1 Powders synthesis*

The oxalate synthesis method was based on previous laboratory works [31, 32]. Quantities of metallic and oxalic salts were adjusted in order to obtain a precursor with the composition (Fe<sub>0.65</sub>Ni<sub>0.35</sub>)C<sub>2</sub>O<sub>4</sub> · 2H<sub>2</sub>O. A 0.55M solution of metallic salts was prepared by dissolving NiSO<sub>4</sub> · 6H<sub>2</sub>O and FeSO<sub>4</sub> · 7H<sub>2</sub>O (purity > 99 wt. %) in deionized water. 1% of sulfuric acid was added in order to prevent oxidation of the ferrous ions. This solution was poured with a peristaltic pump at speed of 20 mL/min, in a 0.2 M

aqueous solution of ammonium oxalate  $(\text{NH}_4)_2\text{C}_2\text{O}_4 \cdot \text{H}_2\text{O}$  (purity > 99 wt. %) to form an oxalate precipitate. After an ageing of 30 minutes under mechanical stirring at 300 rpm, the oxalate suspension was filtered. The precipitate was then washed with deionized water up to remove the adsorbed sulfate ions and dried at 80°C. The dry powder was then manually ground and passed through a 250  $\mu\text{m}$  sieve. A similar procedure was applied for precipitation carried out at the laboratory scale (a few tens of grams) and at the pilot scale (about one kilogram). The oxalate powders were decomposed at 550°C during one hour under a gaseous mixture of 3.9 vol. %  $\text{H}_2$  in nitrogen (50 ppm of oxygen in the gaseous mixture). An ADAMEL tubular furnace equipped with a silica reactor of 2 liters' useful volume was used at the laboratory scale while an ELTI stainless steel muffle furnace of 110 liters' useful volume was used at the pilot scale. After thermal decomposition, the powders were manually ground and passed through a 250  $\mu\text{m}$  sieve.

## *2.2 LPBF processing and thermal post-treatment*

A ProX200 equipment from 3D Systems Company was used for the LPBF process (complies with NF EN ISO/ASTM 52900:2017 standard). This machine was equipped with a 300W Nd:YAG fiber laser with a 1064 nm wavelength. The laser spot was 75  $\mu\text{m}$  in diameter. The build chamber was filled with 3.9 vol. %  $\text{H}_2$  in nitrogen (continuous gas flow between 7 and 10  $\text{L. min}^{-1}$  due to a blind oxygen sensor in the presence of hydrogen). Preliminary experiments were performed in a 1 mm deep AlSi12 aluminum crucible filled with powder. The lased area was 1  $\text{cm}^2$ . The studied parameters were the power of the laser, the scanning speed and the hatch spacing. A conventional raster scanning strategy with a rotation of 90° between the successive layers was applied in this work. The manufacturing of 3D parts was performed on a

steel substrate of 2 cm in diameter, using parameters optimized during AlSi12 crucible tests. Thermal post-treatments at 550 and 1000°C, under 3.9 vol. % H<sub>2</sub> in nitrogen, were also carried out on the 3D parts, using an ADAMEL tubular furnace equipped with a silica reactor.

### *2.3. Characterization*

#### *2.3.1. Phase analysis and determination of the elemental chemical composition*

The nature of the phases of the synthesized powders was determined by X-ray diffraction (XRD) analysis using a Bruker D4-Endeavor diffractometer equipped with a copper anode and a LynxEye 1D detector. LPBF processed 3D parts were analyzed in the Bragg-Brentano configuration using a Bruker D8 diffractometer equipped with a LynxEye 1D detector. Data were recorded using the Cu-K<sub>α</sub> wavelength radiation (40 kV, 40 mA) and collected at room temperature with a 0.016step scan and 55 s/step. Whatever was the diffractometer used, nickel filter was used to eliminate the K<sub>β</sub>-ray and reduce fluorescence. The lattice parameter of the phases present in the synthesized powders was calculated by a Rietveld refinement in the Fullprof program. The elemental chemical composition was determined using three methods: energy dispersive spectroscopy (local EDX analysis with a measurement error of ± 2 wt. %) using an Oxford Instruments X-Max 50 mm<sup>2</sup> detector coupled with scanning electron microscope, X-ray fluorescence (measurement error of ± 5 wt. %) using a Bruker S2 Ranger apparatus and Inductively Coupled Plasma-Atomic Elementary Spectrometry (ICP-AES analysis with a measurement error of ± 2 wt. %).

### *2.3.2. Thermogravimetric analysis*

The thermal decomposition of the metal oxalate powder was followed by thermogravimetric analysis using a Setaram TG 92 equipment. The sample, placed in a platinum crucible, was heated at  $2.5^{\circ}\text{C}\cdot\text{min}^{-1}$  up to  $600^{\circ}\text{C}$  with a dwell of two hours, under 3.9 vol. %  $\text{H}_2$  in nitrogen. A blank test was carried out beforehand in order to eliminate the apparent mass gain due to Archimedes' buoyancy and thus correct the baseline.

### *2.3.3. Specific surface area of the powders*

Measurements were performed with an automatic Micromeritics Flow Sorb II 2300 instrument. The determination of the volume of nitrogen adsorbed at 78K led to the calculation of the specific surface area of the powders according to the theory of Brunauer, Emmett and Teller (BET method). Before any measurement, the powders were degassed under nitrogen flow at  $150^{\circ}\text{C}$  during 1 hour. The accuracy of the measurements is about 10%.

### *2.3.4. Microstructural, physicochemical and rheological characterization*

The synthesized powders were observed with a scanning electron microscope JEOL JSM 6400. The microstructure of the LPBF processed parts, raw and thermally post-treated, was observed with a scanning electron microscope TESCAN VEGA 3 and a MEB-FEG JEOL JSM-7800F Prime apparatus. An X-ray micro-tomography study was performed using a Nanotom 180 device from Phoenix. A  $100\text{ mm}^2$  and 6 mm thick sample was thus analyzed with a tungsten target using a voltage of 140kV, an intensity of  $110\ \mu\text{A}$  and an exposure time of 750 ms per projection. The volume reconstruction was done using DATOS-X software and image processing with VG studio Max 2.1 software. The real density of the powders was measured with a helium pycnometer

AccuPyc II 1340 from Micromeritics. Measurements of apparent and packed densities and of the angle of repose of the composite powder were carried out using respectively a volumeter Electrolab EV02 (complies with ASTM B329-06 and USP 41-616 specifications), a jolting volumeter LSCI IVOL-03 (complies with DIN 53194 standard) and a powder flow tester Electrolab EFT-01 (complies with European Pharmacopoeia specifications).

#### *2.3.5. Measurement of the coefficient of thermal expansion*

The coefficient of thermal expansion (CTE) values were measured on the metal Fe-Ni powder synthesized at the laboratory scale and sintered at 1300°C during one hour under 3,9 vol. % H<sub>2</sub> in nitrogen, on a LPBF processed part, raw and then thermally post treated. A thermomechanical analyzer (TMA) Setaram Setsys evolution 16/18 was used. The three samples were heated at 5°C. min<sup>-1</sup> up to 300°C, under 3,9% vol. H<sub>2</sub> in nitrogen and an applied load of 200 grams. For the LPBF processed samples, alumina plates were positioned in either side to ensure a flat contact surface. A blank test, only performed with the alumina plates, was then subtracted from that of the sample during data processing.

#### *2.3.6. Magnetic and optical characterization*

The magnetic characteristics were determined using a vibrating sample magnetometer (VSM) Quantum Design Versalab. Polymer sample holders were used for powders and LPBF processed parts were stucked on quartz sample holder. The optical properties of the powder used for additive manufacturing were determined by a Bentham PVE 300 photovoltaic characterization system, with integrating operation mode.

### 2.3.7. Measurement of the arithmetic roughness

The arithmetic roughness of the laser processed parts, raw and thermally post-treated, was measured using a 3D confocal microscope S-Neox from Sensofar.

## 3. Results and discussion

### 3.1. Synthesis of metal Fe-Ni powders at the laboratory scale

#### 3.1.1. Metal oxalate precursor

The X-ray diffraction pattern of the oxalate precursor clearly shows in Fig. 1(a) a single peaks system similar to that of  $\beta$ -FeC<sub>2</sub>O<sub>4</sub> · 2H<sub>2</sub>O (JCPDS 00-022-0635), which could be attributed to the formation of a mixed oxalate  $\beta$ -(Fe<sub>1-x</sub>Ni<sub>x</sub>)C<sub>2</sub>O<sub>4</sub> · 2H<sub>2</sub>O. The crystallites size was determined from Scherrer's formula using Eq. (1) and was averaged by taking into account five peaks with a diffraction angle ( $2\theta$ ) between 18 and 44 degrees.

$$L_c = (K \cdot \lambda) / (H \cdot \cos\theta) \quad (1)$$

where  $L_c$  is the crystallites size (nm),  $K$  is the form factor equal to 0.9 in the case of approximately isotropic crystallites,  $\lambda$  is the wavelength (nm) of the X-ray radiation equal to 0.15424 nm in the case of Cu(K $\alpha$ ),  $H$  is the half-height widening of the considered (hkl) peak (rad) and  $\theta$  is the diffraction angle of the considered (hkl) peak (rad).

The small size of the crystallites, about 30 nm, can explain the stabilization of the metastable  $\beta$  form.

SEM micrograph of the oxalate powder reveals in Fig. 1(b) the presence of particles characterized by an approximately spherical shape and a narrow particle size distribution with a medium size near to 11  $\mu$ m. Each particle consists of an agglomerate of polyhedral grains as shown in Fig. 1(c).

The curve characteristic of the thermal decomposition of the oxalate precursor under 3.9 vol. % H<sub>2</sub> in nitrogen clearly shows two steps respectively attributed to dehydration, which ended after three hours at 150°C and decarbonation, which finished at about 500°C (Fig. 2(a)). XRD analysis performed on the decomposition product revealed the formation of a metallic Fe-Ni alloy with a fcc crystallographic structure (Fig. 2(b)). The chemical composition of the metallic powder is near of that of Invar Fe<sub>64</sub>Ni<sub>36</sub> alloy (Table 1). These results confirm that the metallic ions were introduced in the oxalate lattice in the desired proportion: (Fe<sub>0.65</sub>Ni<sub>0.35</sub>)C<sub>2</sub>O<sub>4</sub> · 2H<sub>2</sub>O. The experimental value of the total weight loss (68.54 wt. %) is close to the theoretical one (68.57 wt. %) determined from reaction (2).



**Table 1**

Chemical composition of the Fe-Ni alloy powder obtained by thermal decomposition of the oxalate precursor

Analysis type	EDX	X-ray Fluorescence	ICP-AES
% wt. Fe	64.5*	63.1*	63.8*
% wt. Ni	35.5*	36.9*	36.2*

\* The medium value issued from the three analyses give rise to the following chemical composition: Fe 63.8 wt. % (64.9 at. %), Ni 36.2 wt. % (35.1 at. %).

### 3.1.2. Metal Fe-Ni alloy powders

According to thermogravimetric analysis which revealed that thermal decomposition of the oxalate precursor was completed around 500°C (Fig. 2(a)) and the phase diagram of

the Fe-Ni alloys which indicates that Fe-Ni alloy of Invar composition can be obtained above 460°C [26], thermal decomposition of the oxalate precursor was performed from 500 to 600°C during one hour under 3.9 vol. % H<sub>2</sub> in nitrogen, in order to determine the crystallographic structure and the microstructural evolution (shape and size) of the metallic particles. The results presented in Table 2 reveal that at or below 525°C, a mixture of  $\alpha$ -Fe-Ni and  $\gamma$ -Fe-Ni alloys coexists. On the contrary, thermal decomposition performed at or above 550°C gives rise to a pure  $\gamma$ -Fe-Ni phase.

**Table 2**

Nature of the metallic phases obtained by thermal decomposition of the oxalate precursor

T <sup>a</sup> (°C)	500	500	525	550	600
H <sup>b</sup> (°C/h)	150	75 up to 350°C 150 up to 500°C	150	150	150
XRD	$\gamma$ -Fe-Ni +	$\gamma$ -Fe-Ni +	$\gamma$ -Fe-Ni +	$\gamma$ -Fe-Ni	$\gamma$ -Fe-Ni
Analyses	$\alpha$ -Fe-Ni <sup>c</sup>	$\alpha$ -Fe-Ni <sup>c</sup>	$\alpha$ -Fe-Ni <sup>c</sup>		

<sup>a</sup>Temperature, <sup>b</sup>Heating rate, <sup>c</sup>Minority metallic phase. The  $\gamma$ -Fe-Ni and  $\alpha$ -Fe-Ni alloys respectively present a fcc and bcc crystallographic structure.

The thermal decomposition of the oxalate precursor is pseudomorph (Fig. 3(a)). However, as shown in Fig. 3(b), it induces an opening similar to that of nut shells, or even some fragmentation of the particles due to the release of carbon dioxide gas during the decarbonation step. In order to spread out the CO<sub>2</sub> gas departure in time and thus limit the morphological changes, the heating rate was decreased from 150 to 75°C/h

over the 25-350°C temperature range, in agreement with Figure 2(a). This decrease was however not high enough to prevent or even limit the opening of the particles whose morphology remains similar to that observed in Figure 3(b). The metallic particles synthesized at 550°C are relatively well dispersed (Fig. 3(a)), contrary to the particles obtained at 600°C for which a strong agglomeration was observed in Fig. 3(c). In order to study metal particles in additive manufacturing, the decomposition temperature of 550°C was chosen. The medium size of the metallic particles is about 7 µm.

The X-ray diffraction pattern of the metallic powder obtained by thermal decomposition at 550°C of the mixed oxalate reveals in Fig. 3(d) a single peaks system similar to that of  $\gamma$ -Fe<sub>64</sub>Ni<sub>36</sub> (JCPDS 00-047-1405). The lattice parameter, equal to  $0.3592 \pm 10^{-4}$  nm, corresponds to that of the Invar alloy.

The real density of the metallic powder is equal to 7.898 g. cm<sup>-3</sup>. Considering that the Invar particles are covered by a protective oxide layer similar to Fe<sub>3</sub>O<sub>4</sub> (presence of a very small peak characteristic of the oxygen element on the EDX spectrum) and that open porosity is only present, the purity (p) of the synthesized  $\gamma$ -Fe<sub>64</sub>Ni<sub>36</sub> powder, determined from Eq. (3), is equal to 95 wt.%.

$$\rho_{\text{powder}} = m_{\text{powder}} / v_{\text{powder}} = 7.898 \quad (3)$$

$$= \{[(1-x) \cdot M_{\text{alloy}}] + [x \cdot M_{\text{oxide}}]\} / \{[(1-x) \cdot (M_{\text{alloy}}/\rho_{\text{alloy}})] + [x \cdot (M_{\text{oxide}}/\rho_{\text{oxide}})]\}$$

where  $M_{\text{alloy}}$  is the molar mass of Fe<sub>0.65</sub>Ni<sub>0.35</sub> equal to 56.85 g. mol<sup>-1</sup>,  $M_{\text{oxide}}$  is the molar mass of Fe<sub>3</sub>O<sub>4</sub> equal to 231.55 g. mol<sup>-1</sup>,  $\rho_{\text{alloy}}$  is the real density of Fe<sub>0.64</sub>Ni<sub>0.36</sub> equal to 8.12 g. cm<sup>-3</sup> and  $\rho_{\text{Fe}_3\text{O}_4}$  is the real density of Fe<sub>3</sub>O<sub>4</sub> equal to 5.20 g. cm<sup>-3</sup>.

$$\text{Thus, } x = 12.85 \cdot 10^{-3} \text{ and } p = \{(1-x) \cdot M_{\text{alloy}}\} / \{[(1-x) \cdot M_{\text{alloy}}] + [x \cdot M_{\text{oxide}}]\} = 0.95.$$

The presence of magnetite (5 wt.%) was not observed in Fig. 3(d). This could be attributed to a small size of the Fe<sub>3</sub>O<sub>4</sub> crystallites and to their amorphous or very little

crystallized state, as already shown in the case of superparamagnetic particles of substituted magnetite obtained by thermal decomposition at 500°C of a mixed oxalate precursor [33].

The measurement of magnetization versus magnetic field, performed at 300K with a maximum applied magnetic field of 2T, of the Invar powder synthesized at 550°C gave rise to values of the coercive field about 50. ( $10^3/4\pi$ ) A/m and of the saturation magnetization [estimated for  $1/H = 0$  from the curve  $M = f(1/H)$ ] equal to 117.7 A. m<sup>2</sup>/kg.

Based on the real density measurements, which estimated the purity of the Invar powder (Invar metal particles covered by a protective Fe<sub>3</sub>O<sub>4</sub> layer) around 95 wt.%, the overall value of the saturation magnetization of the Invar powder allowed to determine the real value of the saturation magnetization of the Invar metal particles (Eq. 4).

$$M_s(\text{Invar powder}) = [p \cdot M_s(\text{Fe}_{64}\text{Ni}_{36})] + [(1-p) \cdot M_s(\text{Fe}_3\text{O}_4)] \quad (4)$$

where  $M_s(\text{Invar powder})$  is equal to 117.7 A. m<sup>2</sup>/kg,  $p$  is the mass proportion of Fe<sub>64</sub>Ni<sub>36</sub> equal to 0.95,  $(1-p)$  is the mass proportion of Fe<sub>3</sub>O<sub>4</sub> equal to 0.05,  $M_s(\text{Fe}_3\text{O}_4)$  is the saturation magnetization of the magnetite particles.

The saturation magnetization of the magnetite particles was determined from magnetic characteristics at 300K of an intimate mixture ( $H_c = 180 \cdot (10^3/4\pi)$  A/m,  $M_s = 102.9$  A. m<sup>2</sup>/kg) of  $\alpha$ -Fe metallic iron (13.3 wt. %,  $M_s = 217.2$  A. m<sup>2</sup>/kg) and Fe<sub>3</sub>O<sub>4</sub> magnetite (86.7 wt. %), synthesized from thermal decomposition at 550°C under 3.9 vol. % H<sub>2</sub> in nitrogen of an iron oxalate  $\beta$ -FeC<sub>2</sub>O<sub>4</sub> · 2H<sub>2</sub>O. The obtained value equal to 85.4 A. m<sup>2</sup>/kg is in agreement with that obtained in the literature for Fe<sub>3</sub>O<sub>4</sub> type particles synthesized by the oxalate precursor route [34].

From Eq. (4), the real value of the saturation magnetization of the Invar metal particles is thus equal to 119.4 A. m<sup>2</sup>/kg.

The CTE value of the metallic Fe<sub>64</sub>Ni<sub>36</sub> powder compacted at 250 MPa and then sintered at 1300°C during one hour under 3.9 vol. % H<sub>2</sub> in nitrogen (relative density about 90%), is about 2.9. 10<sup>-6</sup> K<sup>-1</sup> (measured between 65 and 170°C). This value is within the CTE range of annealed Invar36 given in the literature (1.6. 10<sup>-6</sup> K<sup>-1</sup> - 4.1. 10<sup>-6</sup> K<sup>-1</sup> for different temperature ranges from 25 to 260°C) [23].

### *3.2. Synthesis of metal Fe-Ni alloy based powder at the pilot scale*

In order to study Fe-Ni based powder in LPBF process which requires a minimum quantity of powder around 1 kilogram, the soft chemistry synthesis process was extrapolated at the pilot scale. Thus, several batches of about 1.3 kg of oxalic precursor and 0.3 kg of Fe-Ni based powder were prepared.

#### *3.2.1. Metal oxalate precursor*

The X-ray diffraction pattern of the oxalate precursor synthesized at the pilot scale (P oxalate) is similar to that of the oxalate precipitated at the laboratory scale (L oxalate, Fig. 1(a)). A single peaks system similar to that of β-FeC<sub>2</sub>O<sub>4</sub>. 2H<sub>2</sub>O (JCPDS 00-022-0635) is revealed. The crystallites size of the P oxalate, determined from Scherrer's formula (Eq. (1)) using five peaks with a diffraction angle (2θ) between 18 and 44 degrees, is similar to that of the L oxalate (30 nm).

SEM micrographs of the P oxalate presented in Fig. 4(a) and (b), reveal the presence of particles approximately spherical in shape and characterized by a narrow size distribution with a medium size near to 13 μm.

The thermal decomposition of the P oxalate, at 550°C during one hour under 3.9 vol. % H<sub>2</sub> in nitrogen, in a silica tubular furnace used at the laboratory scale, only reveals the

formation of a metal  $\gamma\text{-Fe}_{64}\text{Ni}_{36}$  alloy (JCPDS 00-047-1405, Fig. 4(c)). X-ray fluorescence and EDX analyses carried out on the compacted metal powder confirm a chemical composition close to that of Invar: Fe 63.5 wt. %, Ni 36.5 wt. %. In the same way as at the laboratory scale, these results confirm that the precursor synthesized at the pilot scale is a mixed oxalate  $(\text{Fe}_{0.65}\text{Ni}_{0.35})\text{C}_2\text{O}_4 \cdot 2\text{H}_2\text{O}$ .

The chemical and microstructural characteristics of the L and P oxalates being similar, these results attest to the reproducibility of the synthesis process on the kilogram scale.

### *3.2.2. Fe-Ni metal alloy based powder*

The P oxalate powder was thermally decomposed in a muffle furnace of a 110 liters' useful volume, at 550°C during 1h under 3.9 vol. %  $\text{H}_2$  in nitrogen. To allow good renewal of the gas atmosphere, a flow rate of 580 L/h was introduced for a treated mass of mixed oxalate equal to 900 grams. Whatever the batch synthesized, the XRD analyses revealed the presence of a mixture of a  $\gamma\text{-Fe-Ni}$  alloy and  $\text{Fe}_3\text{O}_4$  magnetite (Fig. 4(d)) and not of a nearly pure metallic alloy of Invar composition, as obtained at the laboratory scale (Fig. 4(c)). For 900 grams of decomposed oxalate (about 5 moles), the amount of  $\text{CO}_2$  formed is about 10 moles, i.e. a volume of gas generated about 224 liters at atmospheric pressure. This volume, twice as large as the furnace volume, was not removed fast enough despite a feed gas flow rate of 580 L.  $\text{h}^{-1}$ . This phenomenon was accentuated by the fact that a heating rate of 2.5°C.  $\text{min}^{-1}$  concentrated the release of  $\text{CO}_2$  produced over only thirty minutes and that in muffle furnace, turbulence of gas flow is present. This resulted in an increase in the partial pressure of oxygen above 50 ppm, which gave rise to the formation of residual  $\text{Fe}_3\text{O}_4$ .

A heat treatment carried out on the  $\gamma\text{-Fe-Ni/Fe}_3\text{O}_4$  composite powder, at 550°C during 10 hours under 3.9 vol. %  $\text{H}_2$  in nitrogen, did not allow to reduce the totality of  $\text{Fe}_3\text{O}_4$ .

A mixture of  $\gamma$ -Fe-Ni,  $\alpha$ -Fe-Ni and a low proportion of  $\text{Fe}_3\text{O}_4$ , was obtained. Above  $560^\circ\text{C}$ , FeO was produced by reaction between iron metal present in the Fe-Ni alloys and  $\text{Fe}_3\text{O}_4$  according to the reaction 5 [35]. The wustite phase was stabilized at room temperature probably due to its low granulometry.



On the other hand, a heat treatment carried out on the composite powder compacted at 250MPa, at  $550^\circ\text{C}$  during 10 hours under 3.9 vol. %  $\text{H}_2$  in nitrogen, facilitated the reduction of  $\text{Fe}_3\text{O}_4$  throughout the volume of the compact. The X-ray diffraction pattern shown in Fig. 5(a) reveals the presence of two metallic alloys,  $\gamma$ -Fe-Ni and  $\alpha$ -Fe-Ni. A simultaneous thermal treatment at  $1000^\circ\text{C}$  during 2 hours under 3.9 vol. %  $\text{H}_2$  in nitrogen, allowed the metal species diffusing and led to the formation of a single Invar type metal alloy, as revealed in Fig. 5(b).

Although the reaction kinetics are very different between conventional processes and additive manufacturing, it was undertaken to study the  $\gamma$ -Fe-Ni/ $\text{Fe}_3\text{O}_4$  composite powder in additive manufacturing under 3.9 % vol.  $\text{H}_2$  in nitrogen, in order to determine the feasibility of producing entirely metallic 3D parts from a single powder consisting of a metal-oxide composite. To our knowledge, no such study has been reported in the literature.

The proportions of metal  $\gamma$ -Fe-Ni alloy and  $\text{Fe}_3\text{O}_4$  present in the composite powder, determined from XRD analysis, are respectively equal to 70 and 30 wt. %. The lattice parameter of the iron oxide, equal to  $0.8397 \pm 10^{-4}$  nm, is close to that of  $\text{Fe}_3\text{O}_4$  (0.8396 nm); thus confirming the presence of pure  $\text{Fe}_3\text{O}_4$  oxide in the composite powder. The lattice parameter of the metal  $\gamma$ -Fe-Ni alloy, equal to  $0.3583 \pm 10^{-4}$  nm, is lower than that of Invar (0.3592 nm).

From lattice parameter value, Vegard's law allowed to determine the proportion of iron and nickel present in the  $\gamma$ -Fe-Ni alloy of the metal-oxide composite powder (Eq. 6).

$$a_{\gamma\text{-Fe-Ni}} = 0.3583 = [x \cdot a_{\text{Ni}}] + [(1-x) \cdot a_{\gamma\text{-Fe}}] \quad (6)$$

where  $x$  is the nickel atomic proportion,  $(1-x)$  is the iron atomic proportion,  $a_{\text{Ni}}$  is the Ni lattice parameter equal to 0.3524 nm (JCPDS 00-004-0850) and  $a_{\gamma\text{-Fe}}$  is the  $\gamma$ -Fe lattice parameter equal to 0.3640 nm [36].

It was thus obtained:  $x = 0.491$  and  $(1-x) = 0.509$ .

From Eq. (6), the Ni and Fe atomic proportions present in the  $\gamma$ -Fe-Ni alloy are respectively about 49 at. % (50 wt. %) and 51 at. % (50 wt. %). The weight composition of the  $\gamma$ -Fe-Ni alloy thus corresponds to  $\gamma\text{-Fe}_{50}\text{Ni}_{50}$ .

The measurement of magnetization versus magnetic field, at 300K with a maximum applied magnetic field of 3T, of the  $\gamma\text{-Fe}_{50}\text{Ni}_{50}\text{-Fe}_3\text{O}_4$  composite powder, revealed values of the coercive field about  $100 \cdot (10^3/4\pi)$  A/m and of the saturation magnetization [estimated at  $1/H = 0$  from the curve  $M_s = f(1/H)$ ] about  $128.5 \text{ A}\cdot\text{m}^2/\text{kg}$ . Considering Eq. (7) and the weight proportions of the two phases present in the composite powder, the  $M_s$  value of the powder allowed determining the saturation magnetization of the metal  $\gamma\text{-Fe}_{50}\text{Ni}_{50}$  alloy.

$$M_s(\gamma\text{-Fe}_{50}\text{Ni}_{50}/\text{Fe}_3\text{O}_4) = [0.7 \cdot M_s(\gamma\text{-Fe}_{50}\text{Ni}_{50})] + [0.3 \cdot M_s(\text{Fe}_3\text{O}_4)] \quad (7)$$

where  $M_s(\gamma\text{-Fe}_{50}\text{Ni}_{50}/\text{Fe}_3\text{O}_4)$  and  $M_s(\text{Fe}_3\text{O}_4)$  are respectively equal to 128.5 and  $85.4 \text{ A}\cdot\text{m}^2/\text{kg}$ .

From Eq. (7),  $M_s(\gamma\text{-Fe}_{50}\text{Ni}_{50})$  is thus equal to  $147 \text{ A}\cdot\text{m}^2/\text{kg}$ .

The saturation magnetization of  $147 \text{ A}\cdot\text{m}^2/\text{kg}$  is in the range of values obtained by Liu et al. [37] in the case of  $\gamma\text{-Fe}_{50}\text{Ni}_{50}$  alloy nanocrystalline powders synthesized via solution combustion process followed by hydrogen reduction at  $500^\circ\text{C}$  ( $144.2 \text{ emu/g}$ )

and 600°C (150.63 emu/g; 1 emu/g in CGS is equal to 1 A.m<sup>2</sup>/kg in SI). Moreover, the saturation magnetization values of  $\gamma$ -Fe<sub>50</sub>Ni<sub>50</sub> and  $\gamma$ -Fe<sub>64</sub>Ni<sub>36</sub>, given in the literature, are respectively equal to 1.6 and 1.3 Tesla [38]. The ratio (1.6/1.3) close to 1.231 is similar to that measured in this work for the  $\gamma$ -Fe<sub>50</sub>Ni<sub>50</sub> and  $\gamma$ -Fe<sub>64</sub>Ni<sub>36</sub> alloys (147.0/119.4).

The real density of the  $\gamma$ -Fe<sub>50</sub>Ni<sub>50</sub>/Fe<sub>3</sub>O<sub>4</sub> composite powder is equal to 7 g. cm<sup>-3</sup>. According to Eq. 8, the quantities of  $\gamma$ -Fe<sub>50</sub>Ni<sub>50</sub> (p) and Fe<sub>3</sub>O<sub>4</sub> (1-p) present in the metal-oxide composite powder are respectively equal to 69 and 31 wt. %. These values are very close to those determined from XRD analysis.

$$\rho_{\text{powder}} = m_{\text{powder}} / v_{\text{powder}} = 7 \quad (8)$$

$$= \{[(1-x) \cdot M_{\text{alloy}}] + [x \cdot M_{\text{oxide}}]\} / \{[(1-x) \cdot (M_{\text{alloy}}/\rho_{\text{alloy}})] + [x \cdot (M_{\text{oxide}}/\rho_{\text{oxide}})]\}$$

where  $M_{\text{alloy}}$  is the molar mass of Fe<sub>0.51</sub>Ni<sub>0.49</sub> equal to 57.25 g. mol<sup>-1</sup>,  $M_{\text{oxide}}$  is the molar mass of Fe<sub>3</sub>O<sub>4</sub> equal to 231.55 g. mol<sup>-1</sup>,  $\rho_{\text{alloy}}$  is the real density of Fe<sub>0.50</sub>Ni<sub>0.50</sub> equal to 8.30 g. cm<sup>-3</sup> and  $\rho_{\text{Fe}_3\text{O}_4}$  is the real density of Fe<sub>3</sub>O<sub>4</sub> equal to 5.20 g. cm<sup>-3</sup>.

Thus,  $x = 10^{-2}$  and  $p = \{(1-x) \cdot M_{\text{alloy}}\} / \{[(1-x) \cdot M_{\text{alloy}}] + [x \cdot M_{\text{oxide}}]\} = 0.69$ .

Although pilot scale thermal decomposition of the P oxalate precursor led to the formation of a metal-oxide composite powder, the transformation is pseudomorph. As shown in Fig. 6(a), the particles remain approximately spherical in shape and their medium size is about 7  $\mu$ m. An opening of the particles was also observed in Fig. 6(b).

After coating the composite particles in a carbon loaded resin and polishing the surface, SEM observations (backscattered electrons mode) revealed an original two-phase microstructure made of an intimate mixture of Fe<sub>50</sub>Ni<sub>50</sub> and Fe<sub>3</sub>O<sub>4</sub> submicronic grains (Fig. 6(c)). Local EDX analyses performed on grey areas only revealed the presence of iron and oxygen. These areas are thus attributed to Fe<sub>3</sub>O<sub>4</sub>. The white areas are only constituted of iron and nickel which confirm the presence of metal Fe-Ni alloy. The

average weight proportions, equal to 53 wt. % Fe and 47 wt. % Ni, are close to those determined from the lattice parameters values and magnetic measurements ( $\text{Fe}_{50}\text{Ni}_{50}$ ). Global EDX analyses performed on the total surface of the particles revealed weight proportions around 67 wt.% Fe and 33 wt. % Ni which are coherent with those introduced during the chemical process (63.5 wt.% Fe and 36.5 wt. % Ni).

The specific surface area of the composite powder is equal to  $6 \text{ m}^2 \cdot \text{g}^{-1}$ . This value is twice higher than that of the  $\text{Fe}_{64}\text{Ni}_{36}$  Invar powder ( $2.7 \text{ m}^2 \cdot \text{g}^{-1}$ ). This could be explained by the submicronic size of the composite grains which induced an increase in the porous volume and a modification of the pore distribution on the surface of the particles.

Measurements of apparent and packed density of the  $\gamma\text{-Fe}_{50}\text{Ni}_{50}/\text{Fe}_3\text{O}_4$  composite powder, gave rise to values about  $0.87 \pm 0.01 \text{ g} \cdot \text{cm}^{-3}$  and  $1.53 \pm 0.01 \text{ g} \cdot \text{cm}^{-3}$ . Hausner's index (packed density / apparent density) and Carr's index ( $100[\text{packed density} - \text{apparent density}]/\text{packed density}$ ) are respectively equal to 1.76 and 43. These values reveal that the composite powder is of the type cohesive. Moreover, the angle of repose value, close to  $42 \pm 1$  degrees, is characteristic of passable flow properties which do not seem to be favorable for obtaining a very dense powder bed in additive manufacturing.

At the wavelength of the Nd:YAG fiber laser of the 3D Systems ProX200 equipment used in this work ( $\lambda=1064 \text{ nm}$ ), the metal-oxide composite powder present a good optical absorbance equal to 77 %.

### *3.3. Manufacturing of Fe-Ni alloy 3D parts using LPBF process and thermal post-treatment*

#### *3.3.1. Behavior in LPBF process of the metal-oxide composite powder. Feasibility tests in AlSi12 crucibles*

##### *3.3.1.1. Laser processing*

The  $\gamma$ -Fe<sub>50</sub>Ni<sub>50</sub>/Fe<sub>3</sub>O<sub>4</sub> composite powder was dried at 80°C during 12h to remove water and other species adsorbed on the grains surface, responsible of the cohesive state of the powder. This one was placed in an AlSi12 crucible of 2 cm in diameter and 1 mm deep. The flatness of the surface was obtained by exerting a slight pressure with a glass slide, which therefore induces a slight compaction of the powder. Whatever the laser parameters studied, a surface of 1 cm<sup>2</sup> was exposed to the laser source, under 3.9 vol. % H<sub>2</sub> in nitrogen.

For power values upper than 75W, a scanning speed equal to 100 mm. s<sup>-1</sup> and hatch spacing values between 10 μm and 60 μm, powder ejection was observed. The energy per unit surface area (Eq. 9) is then respectively upper than 12.5 and 75 J. mm<sup>-2</sup>.

$$E_s = P / v \cdot h \quad (9)$$

where E<sub>s</sub> is the 2D energy density (J. mm<sup>-2</sup>), P is the laser power (J. s<sup>-1</sup>), v is the scanning speed (mm. s<sup>-1</sup>) and h is the hatch spacing (mm).

According to Harrison et al. [23], in the case of high energy densities applied for metal Invar powder, the generated surface temperature can exceed the evaporation temperature of the alloy leading to vaporization recoil, which ejects particles and molten material from the heat-affected area resulting in large irregular voids. For Qiu et al. [39], the driving force for the melt splashing is believed to be due to combined effects including the Marangoni force developed at the surface and subsurface regions of the

melt pool, recoil pressure due to material evaporation and gas expansion. According to these authors [39], the interaction between the laser beam and melt pool is particularly violent (significant melt splashing) when thick powder layers, beyond 60  $\mu\text{m}$ , were processed. This suggests that the melt flow may have become unstable when thicker powder layers were processed by LPBF. The melting temperature of  $\text{Fe}_3\text{O}_4$  being equal to  $1597^\circ\text{C}$  and that of  $\text{Fe}_{50}\text{Ni}_{50}$  being upper than  $1430^\circ\text{C}$  ( $T_{\text{F Ni}}=1455^\circ\text{C}$ ,  $T_{\text{F Fe}}=1538^\circ\text{C}$ ,  $T_{\text{F Invar}}=1427^\circ\text{C}$ ), it is then reasonable to assume that temperatures at least equal to  $1500^\circ\text{C}$  were reached during additive manufacturing of the  $\gamma\text{-Fe}_{50}\text{Ni}_{50}/\text{Fe}_3\text{O}_4$  composite powder. These observations are supported by the fact that temperatures about  $1500^\circ\text{C}$  were exceeded during the additive manufacturing of copper-iron oxide composite material [31]. For the first laser parameters studied, the laser processing on powder bed with a thickness of 1 mm is therefore not favorable to avoid or at least to limit ejection of particles and molten material.

Contrary to previous observations, the use of a power between 30 and 75W did not lead to significant ejection of material, although the range of  $E_s$  values remains high between 12.5 and 75  $\text{J. mm}^{-2}$ . It is then suggested that the power density (ratio between the laser power used and the spot laser area) could be the major parameter that governs the material ejection in our case. Before XRD analysis, the laser processed samples were dusted in order to remove the  $\gamma\text{-Fe}_{50}\text{Ni}_{50}/\text{Fe}_3\text{O}_4$  composite powder that remained stuck on the bottom surface. The XRD analysis performed on the top surface of the laser processed samples (surface area of  $1\text{cm}^2$ , thickness lower than 1mm) revealed the presence of a  $\gamma\text{-Fe-Ni}$  alloy,  $\text{Fe}_3\text{O}_4$  and  $\text{FeO}$ . The presence of wustite could be issued from the reduction of  $\text{Fe}_3\text{O}_4$  by hydrogen present in the gaseous flow according to the

reaction 10 or from the reaction (5) above 560°C between iron atoms of the  $\gamma$ -Fe-Ni alloy and  $\text{Fe}_3\text{O}_4$ .



For a laser power equal to 45W, values of scanning speed and hatch spacing respectively between 1000-2000  $\text{mm. s}^{-1}$  and 15-50  $\mu\text{m}$ , XRD analysis performed on the top surface only revealed the presence of  $\gamma$ -Fe-Ni and FeO. A lack of melting/sintering was however observed, which makes the samples very brittle. The objective of decreasing the hatch spacing would be to increase the time during which the powder bed can be maintained at high temperature, thus allowing the progression of the reduction of the iron ions towards metal iron. A decrease in the hatch spacing value up to 3-7  $\mu\text{m}$  associated with a modification of the studied scanning speed between 1500 and 2250  $\text{mm. s}^{-1}$ , gave rise to the formation of cohesive samples. However, XRD analysis always revealed the peaks characteristic of the wustite phase, in addition to those of a  $\gamma$ -Fe-Ni alloy.

For a constant value of the scanning speed equal to 2000  $\text{mm. s}^{-1}$ , values of power and hatch spacing respectively between 39-48 W and 1-7  $\mu\text{m}$ , the XRD analysis of the top surface showed a strong decrease in the FeO proportion. In particular, for different samples treated with the same laser parameters: power 45W, scanning speed 2000  $\text{mm.s}^{-1}$ , hatch spacing 5  $\mu\text{m}$  (noted 45-2000-5), the X-ray diffraction patterns reveal for the majority of the samples, the presence of a single phase  $\gamma$ -Fe-Ni as shown in Fig. 7(a). A very low proportion of FeO is observed in addition of  $\gamma$ -Fe-Ni for a minority of the samples. On the other hand, the FeO phase is present in the bottom surface (Fig. 7(b)) of all the laser processed samples, regardless of the parameters studied. A second

laser pass performed on the sample 45-2000-5 did not allow removing the FeO phase throughout the sample volume.

SEM micrographs of the top surface of a 45-2000-5 sample containing a very low proportion of FeO are presented in Fig. 8. SEM observations associated with EDX analysis revealed the presence of wustite grains, isolated from each other (B areas, Fig. 8(a) and (c)), on the surface of the micrometric  $\gamma$ -Fe-Ni alloy grains (A areas, Fig. 8(a) and (b)). The medium composition of the alloy, determined from EDX analysis, is about 47 wt. % Fe and 53 wt. Ni. The metal  $\gamma$ -Fe<sub>47</sub>Ni<sub>53</sub> alloy particles present in the laser processed 45-2000-5 sample are therefore slightly enriched in nickel compared to the initial composition of the alloy present in the  $\gamma$ -Fe<sub>50</sub>Ni<sub>50</sub>/Fe<sub>3</sub>O<sub>4</sub> composite powder. The microstructure of the top surface, presented in Fig. 8(d), gives some information about the melt flow behavior. The laser scanned tracks, irregular in shape and discontinuous, do not overlap with neighboring tracks. Open porosity and micro cracks are observed in Fig. 8(d). The majority of the open pores are due to the discontinuity in the tracks; the others in the form of cave-like pores come from the development of overhangs. These observations suggest instability of the melt flow which, according to some authors [39], increases with the powder bed thickness and the scanning speed. These strong surface irregularities induce a very high roughness value about 220  $\mu$ m. Ejection of unmelted powder particles that converted into powder spatters stuck on the surface of the metal  $\gamma$ -Fe-Ni alloy is also shown in Fig. 8(d).

A 45-2000-5 sample, positioned on the side surface, was coated in a carbon loaded resin. The surface was then polished with a diamond suspension which grains size of 6  $\mu$ m, then 3  $\mu$ m. SEM observations of the side surface, performed in a back-scattered electrons mode with contrast of composition, reveal in Fig. 9(a) a densification of the

material, due to heat diffusion by thermal conduction, in a thickness of about 300  $\mu\text{m}$  as well as a difference in chemical composition. The dense upper surface, which appears in white on the micrograph (A area), is constituted of metal alloy with medium composition  $\gamma\text{-Fe}_{45}\text{Ni}_{55}$ . This alloy contains a small dispersion of iron oxide particles of nanometric up to micrometric size (Fig. 9(b)). By analogy with XRD analysis, these particles are attributed to FeO. EDX analysis associated with XRD results revealed that the C area, shown in Fig. 9(a), is constituted of a  $\gamma\text{-Fe}_{47}\text{Ni}_{53}\text{-FeO}$  composite (magnification  $\times 10$  in Fig. 9(c)) containing some microvoids. These analyses confirm a small enrichment of the  $\gamma\text{-Fe-Ni}$  alloy particles in nickel, comparing to the starting metal particles ( $\gamma\text{-Fe}_{50}\text{Ni}_{50}$ ). A border constituted of pure FeO (B area) is also observed in Fig. 9(a) between the predominantly metallic zone and the metal-oxide composite.

This specific microstructure observed in the top surface exposed to laser beam, could be due to Marangoni forces generated by non-uniform surface tensions between the metal and the oxide, themselves due to temperature heterogeneities and thermal gradients resulting from evaporation phenomena [39, 40]. The development of Marangoni forces would thus induce convection flow in the surface and subsurface regions of the melt pool, which in our case would lead to a phase separation between  $\gamma\text{-Fe-Ni}$  and the iron oxide, replacing the metal-oxide composite with a bilayer material. To our knowledge, the transformation under laser processing of a homogeneous metal-oxide composite into a bilayer material consisting of a metal upper layer and an oxide sub-layer has not been revealed in the literature, especially in the case of copper-magnetite composite materials obtained by LPBF processing of a powder mixture [31]. This phenomenon could be explained by the divided state of the composite  $\text{Fe}_{50}\text{Ni}_{50}\text{-Fe}_3\text{O}_4$  powder studied in this work. The increased reactivity of the oxide and metal grains due to their submicron size,

could increase temperature heterogeneities over a larger temperature range and induce high thermal gradients owing to enhanced evaporation; thus increasing Marangoni forces and therefore convection flow in the melt pool.

Phase diagram of the iron species reveals that FeO can be reduced into metal iron at a temperature about 1500°C under 50 ppm of oxygen ( $2.4 \cdot 10^{-7}$  mbar) [41]. However, the presence of metallic iron was not observed by XRD analysis. By assuming that metal iron would be formed from reduction of FeO by hydrogen present in the gaseous flow (3.9 vol. % H<sub>2</sub> in nitrogen) and that it would diffuse in the Fe<sub>50</sub>Ni<sub>50</sub> alloy initially present, this latter would become iron richer. However, EDX analyses revealed enrichment in nickel. These results therefore indicate that the wustite was not reduced to metal iron under this working atmosphere, most certainly due to excessively fast kinetics implemented in the LPBF process, despite the use of a hatch spacing value equal to 5 µm. Indeed, conventional treatments carried out under the same atmosphere have made it possible to reduce iron oxide to metal iron, at 550°C for long holding time of 10 hours.

Similar laser treatments were carried out under pure nitrogen (800 ppm,  $3.8 \cdot 10^{-6}$  mbar). From the iron species phase diagram [41], wustite does not form at this oxygen partial pressure. However, the results are similar to those obtained under weakly hydrogenated atmosphere. This phenomenon confirms that hydrogen has been inactive with respect to the reduction of the iron ions in the used laser process. The formation of FeO results therefore from the reaction (5), whatever the gas studied. The iron atoms present in the initial  $\gamma$ -Fe<sub>50</sub>Ni<sub>50</sub> alloy reacted with the magnetite (30 wt.%) to form the FeO phase. From the reaction (5), this induced a depletion of 5 wt. % Fe in the  $\gamma$ -Fe-Ni alloy, in accordance with that determined by EDX analyses. The final composition of the metal

alloy is then about  $\gamma\text{-Fe}_{45}\text{Ni}_{55}$ . Whatever the laser processing conditions used, the presence of nitride phases was not detected by XRD analysis. Similarly, EDX analyses did not reveal the presence of the nitrogen element.

#### *3.3.1.2. Thermal post-treatment*

Conventional heat treatment under 3.9 vol. %  $\text{H}_2$  in nitrogen, was carried out in two steps on the laser processed 45-2000-5 sample. First, a treatment performed at  $550^\circ\text{C}$  during 10 hours allowed to reduce the wustite phase. As already shown in Fig. 5(a) for the composite powder directly subjected to a conventional heat treatment, a mixture of  $\gamma\text{-Fe-Ni}$  and  $\alpha\text{-Fe-Ni}$  was detected on the top surface of the sample. A simultaneous treatment performed at  $1000^\circ\text{C}$  during five hours gave rise to an inter-diffusion of the two metallic phases. Comparing with Fig. 5(b), XRD analyses carried out on the top surface also revealed a single  $\gamma\text{-Fe-Ni}$  alloy. X-ray fluorescence analysis showed however a different chemical composition between the top and bottom surfaces respectively close to  $\text{Fe}_{50}\text{Ni}_{50}$  and  $\text{Fe}_{66}\text{Ni}_{34}$ . After the post-treatment, the composition of the top surface was slightly iron richer ( $\gamma\text{-Fe}_{50}\text{Ni}_{50}$ ) than that of the laser processed sample due to the reduction of the small proportion of FeO particles dispersed into the dense  $\gamma\text{-Fe}_{45}\text{Ni}_{55}$  alloy (Fig. 9(b)). On the contrary, the reduction of FeO present in the  $\gamma\text{-Fe}_{47}\text{Ni}_{53}\text{-FeO}$  composite, observed in the bottom surface in Fig. 9(c), gave rise to a strong iron enrichment of the Fe-Ni alloy ( $\gamma\text{-Fe}_{66}\text{Ni}_{34}$  close to the Invar composition). The presence of nitride phases or nitrogen element was not detected, respectively by XRD or EDX analyses, in the heat post-treated samples, despite the implementation of long treatments under 3.9 vol. %  $\text{H}_2$  in nitrogen.

By using the same synthesis route based on the implementation of a LPBF process followed by a conventional thermal post-treatment, the additive manufacturing of 3D parts in the form of 1 cm<sup>3</sup> cubes was carried out.

### 3.3.2. Synthesis of metal Fe-Ni alloy 3D parts by LBPF additive manufacturing

#### 3.3.2.1. Laser processing

Owing to its cohesive behavior, the  $\gamma$ -Fe<sub>50</sub>Ni<sub>50</sub>-Fe<sub>3</sub>O<sub>4</sub> composite powder was dried at 80°C during 12 hours in order to prevent it from sticking on the roller and to facilitate its spreading into homogeneous powder bed. Despite the small size of the particles (average size of 7  $\mu$ m) compared to the one recommended in additive manufacturing (15-50  $\mu$ m) and their specific morphology comparable to opened nut shells, it was then possible to obtain powder beds of homogeneous thickness without macroscopic defects by the automatic spreading system of the machine.

By using the laser parameters previously studied (power 45W, scanning speed 2000 mm.s<sup>-1</sup>, hatch spacing 5  $\mu$ m), manufacturing of 1 cm<sup>3</sup> cubes was correctly carried out only for bed thickness between 400 and 500  $\mu$ m. Below 400  $\mu$ m, significant ejection of powder or molten material was observed. Upper 500  $\mu$ m, no coherent parts were prepared. As the power density was unchanged, high values of energy per unit volume (Eq. 11) could explain the ejection phenomenon.

$$E_v = P / v.h.e \quad (11)$$

where  $E_v$  is the 3D energy density (J. mm<sup>-3</sup>),  $P$  is the laser power (J. s<sup>-1</sup>),  $v$  is the scanning speed (mm. s<sup>-1</sup>),  $h$  is the hatch spacing (mm) and  $e$  is the powder bed thickness (mm).

For bed thickness between 50 and 300  $\mu$ m,  $E_v$  is between 15 and 90 J. mm<sup>-3</sup>, against 9 to 11 J. mm<sup>-3</sup> for bed thickness between 400 and 500  $\mu$ m.  $E_v$  values, lower than 11 J. mm<sup>-3</sup>,

are therefore recommended to avoid material ejection. The behavior in LPBF process of the  $\gamma$ -Fe<sub>50</sub>Ni<sub>50</sub>-Fe<sub>3</sub>O<sub>4</sub> composite powder is very different from that of Invar 36 alloy for which  $E_v$  values between 60 and 100 J. mm<sup>-3</sup> allowed to obtain highly densified 3D parts [11].

The 3D parts so-obtained (Fig. 10, bed thickness about 400  $\mu$ m), although being easily manipulated, are relatively brittle and tend to delaminate. As already been shown by Qiu et al. [39], strong surface roughness induced from the discontinuity of the laser scanned tracks can cause inhomogeneous powder spreading and distribution and thus inconsistent melt flow and melt pool in the subsequent layers, resulting in the development of strong porosity in the bulk material as revealed in Fig. 10 (a) and (b). Moreover, due to the fact that each powder bed of the LPBF processed 45-2000-5 samples is constituted by a mainly metallic phase in the top surface (white and bright areas in Fig. 10(c)) and a metal-oxide composite in the bottom one (grey areas in Fig. 10(c)), it become more difficult to have a good adhesion between two adjacent beds. Due to the different coefficients of thermal expansion between an oxide and a metal, cracks can appear between two neighboring powder beds on cooling, which could cause their delamination as shown in Fig. 10(c).

XRD analysis of the top surface presented in Fig.10 (a) and (b) revealed the presence of a metal  $\gamma$ -Fe-Ni alloy associated with a very low proportion of FeO. The characteristic diffraction peaks of  $\gamma$ -Fe-Ni, FeO and Fe<sub>3</sub>O<sub>4</sub> were detected in the side surface shown in Fig. 10 (c) and (d). The presence of magnetite is due to unmelted starting particles in the extreme lower surface of each powder bed, which remained trapped between two adjacent layers because they could not be removed by dusting. SEM observations carried out on the side surface indeed showed the presence of particles in the shape of

nut shells characteristic of the starting  $\gamma$ -Fe<sub>50</sub>Ni<sub>50</sub>-Fe<sub>3</sub>O<sub>4</sub> composite powder (Fig. 10(d)). The presence of unmelted composite powder also did not promote good adhesion between two adjacent laser processed powder beds.

The CTE values of the sample, measured between 20-90°C and 70-200°C, are respectively equal to  $7.5 \cdot 10^{-6} \text{ K}^{-1}$  and  $8.7 \cdot 10^{-6} \text{ K}^{-1}$ . Despite the presence of iron oxides in the LPBF processed sample mainly composed of  $\gamma$ -Fe-Ni alloy (Fe 45-47 wt. %, Ni 53-55 wt. %), these values are slightly lower than that of a pure  $\gamma$ -Fe<sub>52</sub>Ni<sub>48</sub> alloy of similar composition ( $9 \cdot 10^{-6} \text{ K}^{-1}$  measured between 0-100°C) [37].

#### 3.3.2.2. *Thermal post-treatment*

Conventional heat treatment in two steps (550°C-10h followed by 1000°C-5h) was carried out under 3.9 vol. % H<sub>2</sub> in nitrogen, on the 3D parts. XRD analysis of the top surface revealed the presence of a  $\gamma$ -Fe-Ni alloy whereas a mixture of  $\gamma$ -Fe-Ni alloy and  $\alpha$ -Fe-Ni alloys was detected on the side surface.

SEM micrographs of the top surface, presented in Fig. 11(a) and (b) show again a discontinuity of the laser scanned tracks, confirming an instability of the melt pool. This induced a strong roughness value of about 200  $\mu\text{m}$ . The inferior tracks, scanned according to a strategy with a rotation of 90°, are also observed in Fig. 11(b). A difference in microstructure was also revealed at a periodicity along the building z axis, corresponding to the thickness of the powder bed (400  $\mu\text{m}$ ) used in the LPBF process (Fig. 11(b)). This one is clearly highlighted in the micrographs of the side surface shown in Fig. 11 (c) and (e). Each periodic layer of about 400  $\mu\text{m}$  (Fig. 11(c)) is constituted of a dense microstructure in a thickness of about 300  $\mu\text{m}$  (Fig. 11(e)) while a type vermicular porous microstructure (Fig. 11(d) and (e)) composes the bottom in a thickness of about 100  $\mu\text{m}$ . In addition to a difference in microstructure, the presence of

successive strata made of  $\alpha$ - or  $\gamma$ -Fe-Ni alloys of different compositions was revealed from EDX analyses performed within the 400  $\mu\text{m}$  thickness of each periodic layer. This is the result of the thermal post-treatment performed under 3.9 vol. %  $\text{H}_2$  in nitrogen on the LPBF-processed 45-2000-5 samples (Fig. 9(a), 10(c)). The chemical composition of each area, differentiated by a letter in Fig. 9(a) and 11(e), was reported in Table 3 (averaged over ten local EDX analyses). Thermal post-treatment under weakly hydrogenated atmosphere allowed reducing the totality of the residual FeO and  $\text{Fe}_3\text{O}_4$  iron oxides. These reductions associated with diffusion phenomena gave rise, according to the EDX analyzed area, to the formation of  $\alpha$ - or  $\gamma$ -Fe-Ni alloys, in accordance with the mixture of  $\gamma$ -Fe-Ni and  $\alpha$ -Fe-Ni alloys detected by XRD analyses in the side surface. The upper surface of each periodic layer, after reducing the low proportion of FeO particles dispersed into the  $\gamma\text{-Fe}_{45}\text{Ni}_{55}$  matrix (A area), recovered the original  $\gamma\text{-Fe}_{50}\text{Ni}_{50}$  composition (A' area) of the Fe-Ni alloy present in the starting composite powder. Reduction of the FeO oxide constituting the border (B area) associated with some nickel diffusion from the adjacent C area, gave rise to the formation of the  $\alpha\text{-Fe}_{87}\text{Ni}_{13}$  alloy (B' area). Reduction of the FeO oxide associated with diffusion phenomena between the resulting iron metal and the  $\gamma\text{-Fe}_{47}\text{Ni}_{53}$  alloy of the C area, depleted in nickel due its diffusion in moderate quantity toward the adjacent B area, induced the formation of the  $\alpha\text{-Fe}_{70}\text{Ni}_{30}$  alloy (C' area). Finally, reduction of the  $\text{Fe}_3\text{O}_4$  oxide, issued from the  $\gamma\text{-Fe}_{50}\text{Ni}_{50}\text{-Fe}_3\text{O}_4$  composite powder trapped between two adjacent layers (D area), is at the origin of the formation of the D' area characterized by a vermicular type porous microstructure and a  $\gamma\text{-Fe}_{64}\text{Ni}_{36}$  Invar composition. These phenomena thus induced an iron composition gradient from the B' to D' areas (Table 3).

**Table 3**

Chemical composition of the different areas observed in the LPBF processed 45-2000-5 samples and in the same samples thermally post-treated at 1000°C-5h under 3.9% vol. H<sub>2</sub> in nitrogen

Areas observed in the 45-2000-5 samples (see Fig. 9a)	Similar areas observed after thermal post-treatment (see Fig. 11e)
A: Dispersion of 10 wt. % FeO particles in a 90 wt. % dense $\gamma$ -Fe <sub>45</sub> Ni <sub>55</sub> matrix (see also Fig. 8)	A': Dense $\gamma$ -Fe <sub>50</sub> Ni <sub>50</sub> area
B: Dense border of pure FeO located between the A and C areas	B': Dense $\alpha$ -Fe <sub>87</sub> Ni <sub>13</sub> area (after hydrogen reduction of FeO and nickel enrichment about 10 wt. %)
C: Dense 65 wt. % $\gamma$ -Fe <sub>47</sub> Ni <sub>53</sub> -35 wt. % FeO composite	C': Dense $\alpha$ -Fe <sub>70</sub> Ni <sub>30</sub> area (after hydrogen reduction of FeO and nickel depletion about 10 wt. %)
D: Starting 70 wt. % $\gamma$ -Fe <sub>50</sub> Ni <sub>50</sub> 30 wt. % Fe <sub>3</sub> O <sub>4</sub> powder (absent in Fig. 9a owing to dusting but present in Fig. 10c)	D': Vermicular porous $\gamma$ -Fe <sub>64</sub> Ni <sub>36</sub> area (see also Fig. 11d)

The measurement of magnetization versus magnetic field, performed at 300K with a maximum applied magnetic field of 2T, on three LPBF processed 45-2000-5 samples then thermally post-treated, gave rise to medium values of the coercive field about 2.7 ( $10^3/4\pi$ ) A/m and of the saturation magnetization about 160 A.m<sup>2</sup>/kg (Fig. 12). The M<sub>s</sub>

value of  $160 \text{ A.m}^2/\text{kg}$  is comparable to those measured by Chaudhary et al [17] on  $\text{Fe}_{55}\text{Ni}_{45}$  ( $161.6 \text{ emu/g}$ ),  $\text{Fe}_{60}\text{Ni}_{40}$  ( $165.6 \text{ emu/g}$ ) and  $\text{Fe}_{70}\text{Ni}_{30}$  ( $168.7 \text{ emu/g}$ ) alloys obtained by additive manufacturing ( $1 \text{ emu/g}$  in CGS is equal to  $1 \text{ A.m}^2/\text{kg}$  in SI). The value of the coercive field of the multiphase Fe-Ni alloy is about two to three times lower than those measured by Chaudhary et al [17], between 4.9 and 7.9 Oe ( $10 \text{ Oe}$  in CGS is equal to  $1 \cdot (10^3/4\pi) \text{ A/m}$  in SI).

X-ray micro-tomography micrographs carried out on a LPBF processed 45-2000-5 sample then thermally post-treated, are presented in Fig. 13(a) and (b). Open and closed porosities are respectively represented in green and blue in Fig. 13(b); the metallic Fe-Ni alloy being observed in white on this micrograph. The total porosity value is close to 63 vol. %. Despite the presence of an important porosity, LPBF processing followed by heat post-treatment led to the manufacturing of a porous multiphase Fe-Ni alloy parts with good mechanical strength.

The CTE value of the 3D parts, measured between 100 and  $250^\circ\text{C}$ , is about  $6 \cdot 10^{-6} \text{ K}^{-1}$ . This value, although being higher than that of Invar alloy, remains relatively low to allow some applications to be considered in which dimensional stability over a wide range of temperatures would be required.

#### **4. Conclusions**

A  $\gamma\text{-Fe}_{64}\text{Ni}_{36}$  Invar powder was synthesized by thermal decomposition at  $550^\circ\text{C}$  under a weakly hydrogenated atmosphere, of a co-precipitated mixed oxalate  $(\text{Fe}_{0.65}\text{Ni}_{0.35})\text{C}_2\text{O}_4 \cdot 2\text{H}_2\text{O}$ . The particles are approximately spherical in shape and their medium size is about  $7 \mu\text{m}$ . The purity of the metallic particles covered by a protective  $\text{Fe}_3\text{O}_4$  oxide layer is about 95 wt. %. The CTE value, measured between 65 and  $170^\circ\text{C}$ , confirm the presence of metal Invar. Increasing the oxygen partial pressure of the gaseous flow during the

thermal decomposition of the oxalic precursor, induced the formation of a  $\gamma$ - $\text{Fe}_{50}\text{Ni}_{50}/\text{Fe}_3\text{O}_4$  composite powder of a medium size about 7  $\mu\text{m}$ . The composite particles, approximately spherical in shape, present an original microstructure consisting of an intimate mixture of  $\gamma$ - $\text{Fe}_{50}\text{Ni}_{50}$  alloy (70 wt. %) and  $\text{Fe}_3\text{O}_4$  oxide (30 wt. %) submicronic grains. LPBF processing of the composite powder under a weakly hydrogenated atmosphere, allowed to transform  $\text{Fe}_3\text{O}_4$  into  $\text{FeO}$  but the reaction kinetic of laser processes is however too fast to allow hydrogen reduction of the wustite phase into metal iron. The manufacturing of 3D parts, carried out for powder bed thickness between 400 and 500  $\mu\text{m}$ , revealed a specific microstructure in the upper surface of each laser processed powder bed. It results from a phase separation between  $\text{FeO}$  and  $\gamma$ - $\text{Fe}_{45}\text{Ni}_{55}$ , replacing the metal-oxide composite with a dense bilayer material. The presence of residual  $\text{Fe}_3\text{O}_4$  coming from unmelted starting powder, was also detected. A conventional thermal post-treatment carried out on the laser processed parts, under a weakly hydrogenated atmosphere, allowed to reduce the totality of the iron oxides and to obtain by diffusion of the metallic species, metal Fe-Ni 3D parts with a porosity level near to 63 vol. % and a good mechanical strength. Repeatable heterogeneities of microstructure (dense and porous) and of composition (formation of successive layers of different bcc and fcc Fe-Ni alloys including Invar), at a periodicity corresponding to the thickness of the powder bed used in the LPBF process, constitute the hallmark of the LPBF treatment carried out on the  $\text{Fe}_{50}\text{Ni}_{50}\text{-Fe}_3\text{O}_4$  composite powder. The CTE value of the heat post-treated 3D parts, remains relatively low ( $6 \cdot 10^{-6} \text{ K}^{-1}$  between 100 and  $250^\circ\text{C}$ ) to allow some applications to be considered, such as transfer of fluids in porous devices for which high dimensional stability under temperature variation would be required. On the other hand, the soft magnetic properties of the multiphase Fe-Ni alloy

3D parts could suggest potential applications in magnetic devices such as transformers or electric motors. For this purpose, the perspectives of studies would consist in modifying the laser parameters programming to increase the density of the 3D parts while preserving the periodic specific microstructure presented in this paper.

### **Acknowledgements**

This research did not receive any specific grant from funding agencies in the public, commercial, or not-for-profit sectors. The authors thank the Fermat Federation and the Raimond Castaing micro-characterization Center of Toulouse, France, for X-ray microtomography and MEB-FEG observations. They particularly thank Marie-Claire Barthelemy, Benjamin Duployer and Yann Borjon-Piron (CIRIMAT, Toulouse, France) for their technical support, respectively in thermomechanical, X-ray diffraction and EDS analyses.

### **Declaration of Interest Statement**

The authors declare that they have no known competing financial interests or personal relationships that could have appeared to influence the work reported in this paper.

### **References**

[1] H. D. Arnold, G. W. Elmen, Permalloy, a new magnetic material of very high permeability, *Bell System Tech. J.* 2: 3 (1923) 101-111.

<https://doi.org/10.1002/j.1538-7305.1923.tb03595.x>

[2] R. Hamzaoui, O. Elkedim, N. Fenineche, E. Gaffet, J. Craven, Structure and magnetic properties of nanocrystalline mechanically alloyed Fe-10% Ni and Fe-20% Ni, *Mater. Sci. Eng. A* 360 (2003) 299-305.

[https://doi.org/10.1016/S0921-5093\(03\)00460-X](https://doi.org/10.1016/S0921-5093(03)00460-X)

[3] I. Chicinas, O. Geoffroy, O. Isnard, V. Pop, Soft magnetic composite based on mechanically alloyed nanocrystalline Ni<sub>3</sub>Fe phase, *J. Magn. Magn. Mater.* 290-291 (2005) 1531-1534.

<https://doi.org/10.1016/j.jmmm.2004.11.249>

[4] J.M.D. Coey, *Magnetic materials*, *J. Alloys Compd.* 326(1-2) (2001) 2-6.

[https://doi.org/10.1016/S0925-8388\(01\)01239-7](https://doi.org/10.1016/S0925-8388(01)01239-7)

[5] J. Petzold, Advantages of softmagnetic nanocrystalline materials for modern electronic applications, *J. Magn. Magn. Mater.* 242-245 Part1 (2002) 84-89.

[https://doi.org/10.1016/S0304-8853\(01\)01206-9](https://doi.org/10.1016/S0304-8853(01)01206-9)

[6] D.C. Jiles, Recent advances and future directions in magnetic materials, *Acta Mater.* 51 (2003) 5907-5939.

<https://doi.org/10.1016/j.actamat.2003.08.011>

[7] T.N. Lamichhane, L. Sethuraman, A. Dalagan, H. Wang, J. Keller, M.P. Paranthaman, Additive manufacturing of soft magnets for electrical machines-a review, *Mater. Today Phys.* 15 (2020) 100255, 1-23.

<https://doi.org/10.1016/j.mtphys.2020.100255>

[8] J.M. Silveyra, E. Ferrara, D.L. Huber, T.C. Monson, Soft magnetic materials for a sustainable and electrified world, *Science*, 362 (2018) 6413, 1-9.

<https://doi.org/10.1126/science.aao0195>

[9] D.G. Rancourt, M.Z. Dang, Relation between anomalous magnetovolume behavior and magnetic frustration in Invar alloys, *Phys. Rev. B*, 54(17) (1996) 12225-12231.

<https://doi.org/10.1103/PhysRevB.54.12225>

[10] C. Guillaume, Invar and its applications, *Nature*, 71 (1904) 134-139.

<https://doi.org/10.1038/071134a0>

[11] K. Wei, Q. Yang, B. Ling, X. Yang, H. Xie, Z. Qu, D. Fang, Mechanical properties of Invar 36 alloy additively manufactured by selective laser melting, *Mater. Sci. Eng. A* 772 (2020) 138799, 1-9.

<https://doi.org/10.1016/j.msea.2019.138799>

[12] D. Herzog, V. Seyda, E. Wycisk, C. Emmelmann, Additive manufacturing of metals, *Acta Mater.* 117 (2016) 371-392.

<https://doi.org/10.1016/j.actamat.2016.07.019>

[13] H. Asgari, M. Salarian, H. Ma, A. Olubamiji, M. Vlasea, On the thermal expansion behavior of invar alloy fabricated by modulated laser powder bed fusion, *Mater. Des.* 160 (2018) 895-905.

<https://doi.org/10.1016/j.matdes.2018.10.025>

[14] X.C. Li, J. Stampfl, F.R. Prinz, Mechanical and thermal expansion behavior of laser deposited metal matrix composites of Invar and TiC, *Mater. Sci. Eng. A* 282 (1-2) (2000) 86-90.

[https://doi.org/10.1016/S0921-5093\(99\)00781-9](https://doi.org/10.1016/S0921-5093(99)00781-9)

[15] V. Chaudhary, S. A. Mantri, R.V. Ramanujan, R. Banerjee, Additive manufacturing of magnetic materials, *Prog. Mater. Sci.* 114, (2020) 100688, 1-38.

<https://doi.org/10.1016/j.pmatsci.2020.100688>

[16] X. Zhan, Y. Meng, J. Zhou, C. Qi, C. Zhang, D. Gu, Quantitative research on microstructure and thermal physical mechanism in laser melting deposition for Invar alloy, *J. Manufacturing Processes*, 31 (2018) 221-231.

<https://doi.org/10.1016/j.mapro.2017.11.018>

[17] V. Chaudhary, N.M.S.K.K. Yadav, S. A. Mantri, S. Dasari, A. Jagetia, R.V. Ramanujan, R. Banerjee, Additive manufacturing of functionally graded Co-Fe and Ni-

Fe magnetic materials, *J. Alloys Compd.* 823 (2020) 153817, 1-8.  
<https://doi.org/10.1016/j.jallcom.2020.153817>

[18] B. Zhang., N. E. Fenineche, L. Zhu, H. Liao, Ch. Coddet, Studies of magnetic properties of permalloy (Fe-30%Ni) prepared by SLM technology, *J. Magn. Magn. Mater.* 324 (2012) 495-500.  
<https://doi.org/10.1016/j.jmmm.2011.08.030>

[19] B. Zhang., N. E. Fenineche, H. Liao, Ch. Coddet, Microstructure and magnetic properties of Fe-Ni alloy fabricated by selective laser melting Fe/Ni mixed powders, *J. Mater. Sci. Technol.* 29(8), (2013) 757-760.  
<https://doi.org/10.1016/j.jmst.2013.05.001>

[20] B. Zhang., N. E. Fenineche, H. Liao, Ch. Coddet, Magnetic properties of in-situ synthesized FeNi<sub>3</sub> by selective laser melting Fe-80%Ni powders, *J. Magn. Magn. Mater.* 336 (2013) 49-54.  
<https://doi.org/10.1016/j.jmmm.2013.02.014>

[21] C. Qiu, N.J.E. Adkins, M.M. Attallah, Selective laser melting of Invar 36: microstructure and properties, *Acta Mater.* 103 (2016) 382-395.  
<https://doi.org/10.1016/j.actamat.2015.10.020>

[22] M. Yakout, A. Cadamuro, M.A. Elbestawi, S.C. Veldhuis, The selection of process parameters in additive manufacturing for aerospace alloys, *The International J. Adv. Manufacturing Technol.*, 92 (2017) 2081-2098.  
<https://doi.org/10.1007/s00170-017-0280-7>

[23] N.J. Harrison, I. Todd, K. Mumtaz, Thermal expansion coefficients in Invar processed by selective laser melting, *J. Mat. Sci.* 52 (2017) 10517-10525.  
<https://doi.org/10.1007/s10853-017-1169-4>

[24] M. Yakout, M.A. Elbestawi, S.C. Veldhuis, A study of thermal expansion coefficients and microstructure during selective laser melting of Invar 36 and stainless steel 316L, *Additive Manufacturing*, 24 (2018) 405-418.

<https://doi.org/10.1016/j.addma.2018.09.035>

[25] M. Yakout, M.A. Elbestawi, S.C. Veldhuis, Density and mechanical properties in selective laser melting of Invar 36 and stainless steel 316L, *J. Mater. Process. Technol.* 266 (2019), 397-420.

<https://doi.org/10.1016/j.matprotec.2018.11.006>

[26] O. A. Cortez, F. J. Moura, E. De Albuquerque Brocchi, R. N. C. De Siqueira, R. F. M. De Souza, Fe-Ni alloy synthesis based on nitrates thermal decomposition followed by H<sub>2</sub> reduction, *Metall. Mater. Trans. B* 45B (2014), 2033-2039.

<https://doi.org/10.1007/s11663-014-0221-x>

[27] Y. Gao, Z.Y. Li, D. Jin, J. Liu, J.C. Zhai, Preparation and characterization of nano-Fe<sub>50</sub>Ni<sub>50</sub> alloy powder by chemical co-precipitation hydrogen reducing process, *Integrated Ferroelectrics*, 128(1), 2011-54-58.

<https://doi.org/10.1080/10584587.2011.576187>

[28] B. Song, S. Dong, P. Coddet, G. Zhou, S. Ouyang, H. Liao, Ch. Coddet, Microstructure and tensile behavior of hybrid nano-micro SiC reinforced iron matrix composites produced by selective laser melting, *J. Alloys Compd.* 579 (2013) 415-421.

<https://doi.org/10.1016/j.jallcom.2013.06.087>

[29] S. Dadbakhsh, L. Hao, P.G.E. Jerrard, D.Z. Zhang, Experimental investigation on selective laser melting behavior and processing windows of in situ reacted Al/Fe<sub>2</sub>O<sub>3</sub> powder mixture, *Powder Technol.* 231 (2012), 112-121.

<https://doi.org/10.1016/j.powtec.2012.07.061>

[30] S. Dadbakhsh, L. Hao, Effect of hot isostatic pressing (HIP) on Al composite parts made from laser consolidated Al/ Fe<sub>2</sub>O<sub>3</sub> powder mixtures, *J. Mater. Process. Technol.* 212 (2012) 2474-2483.

<https://doi.org/10.1016/j.jmatprotec.2012.06.016>

[31] I. Pasquet, V. Baco-Carles, P. Chamelot, M. Gibilaro, L. Massot, Ph. Tailhades, A multimaterial based on metallic copper and spinel oxide made by powder bed laser fusion: A new nanostructured material for inert anode dedicated to aluminum electrolysis, *J. Mater. Process. Technol.* 278 (2020) 116452, 1-9.

<https://doi.org/10.1016/j.jmatprotec.2019.116452>

[32] V. Baco-Carles, I. Pasquet, V. Laurent, A. Gabriel, Ph. Tailhades, Preparation and electrical properties of dense micro-cermets made of nickel ferrite and metallic copper, *Solid State Sci.* 11 (2009), 1503-1506.

<https://doi.org/10.1016/j.solidstatesciences.2009.05.016>

[33] V. Baco, L. Huguet, M. Gougeon, H. Le Trong, Ph. Tailhades, Material consisting of friable micrometric aggregates comprising nanometric particles, International Patent WO 2016/097568 A1, 23.06.2016.

[34] Ph. Tailhades, Ch. Sarda, Ch. Bonino, P. Mollard, A. Rousset, Magnetic properties of boron and cobalt doped iron oxide pigments prepared from oxalic precursors, *J. Magn. Magn. Mater.* 89(1-2) (1990) 33-37.

[https://doi.org/10.1016/0304-8853\(90\)90703-S](https://doi.org/10.1016/0304-8853(90)90703-S)

[35] V. Carles, P. Alphonse, Ph. Tailhades, A. Rousset, Study of thermal decomposition of FeC<sub>2</sub>O<sub>4</sub>.2H<sub>2</sub>O under hydrogen, *Thermochim. Acta*, 334 (1999) 107-113.

[https://doi.org/10.1016/S0040-6031\(99\)00133-1](https://doi.org/10.1016/S0040-6031(99)00133-1)

[36] B. Song, S. Dong, S. Deng, H. Liao, Ch. Coddet, Microstructure and tensile properties of iron parts fabricated by selective laser melting, *Optics and Laser Technol.* 56 (2014) 451-460.

<https://doi.org/10.1016/j.optlastec.2013.09.017>

[37] Y. Liu, M. Qin, L. Zhang, M. Huang, S. Li, B. Jia, D. Zhang, X. Qu, Solution combustion synthesis of nanocrystalline Fe-50%Ni alloy powder, *Powder Technol.* 267 (2014), 68-73.

<https://doi.org/10.1016/j.powtec.2014.07.003>

[38] G. Couderchon, Alliages fer-nickel et fer-cobalt, propriétés magnétiques, *Techniques de l'Ingénieur (France) D2130* (1994), p. 10.

[39] C. Qiu, C. Panwisawas, M. Ward, H. C. Hector, C. Basoalto, J. F. Brooks, On the role of melt flow into the surface structure and porosity development during selective laser melting, *Acta Mater.* 96 (2015) 72-79.

<https://doi.org/10.1016/j.actamat.2015.06.004>

[40] C. Panwisawas, C. L. Qiu, Y. Sovani, J. W. Brooks, M. M. Attallah, H. C. Basoalto, On the role of thermal fluid dynamics into the evolution of porosity during selective laser melting, *Scripta Mater.* 105 (2015), 14-17.

<https://doi.org/10.1016/j.scriptamat.2015.04.016>

[41] G. Ketteler, W. Weiss, W. Ranke, R. Schlögl, Bulk and surface phases of iron oxides in an oxygen and water atmosphere at low pressure, *Phys. Chem. Chem. Phys.* 3 (2001) 1114-1122.

<https://doi.org/10.1039/b009288f>

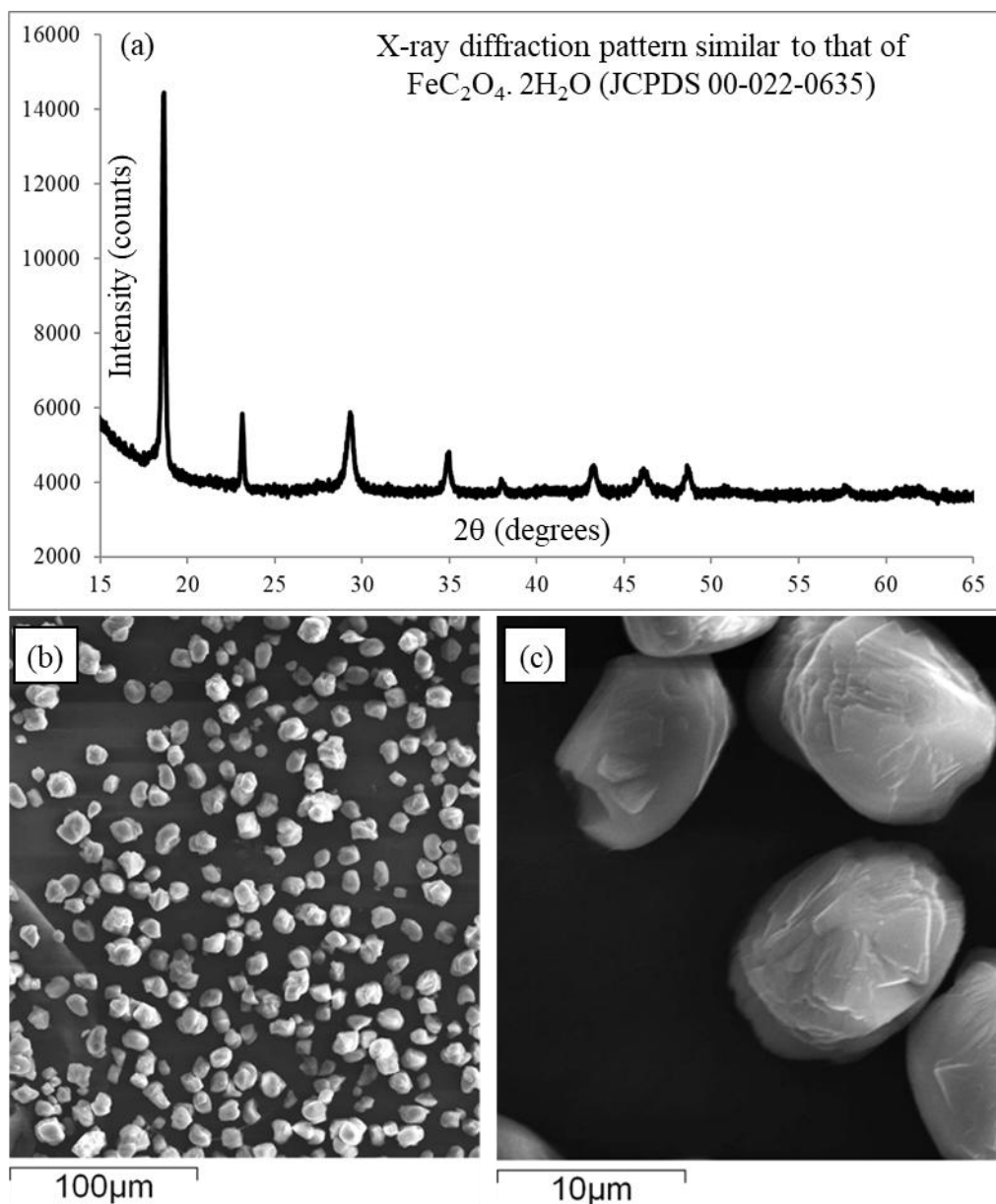


**Figure 1.** Oxalate precursor synthesized at the laboratory scale (a) X-ray diffraction pattern, (b) and (c) SEM micrographs.

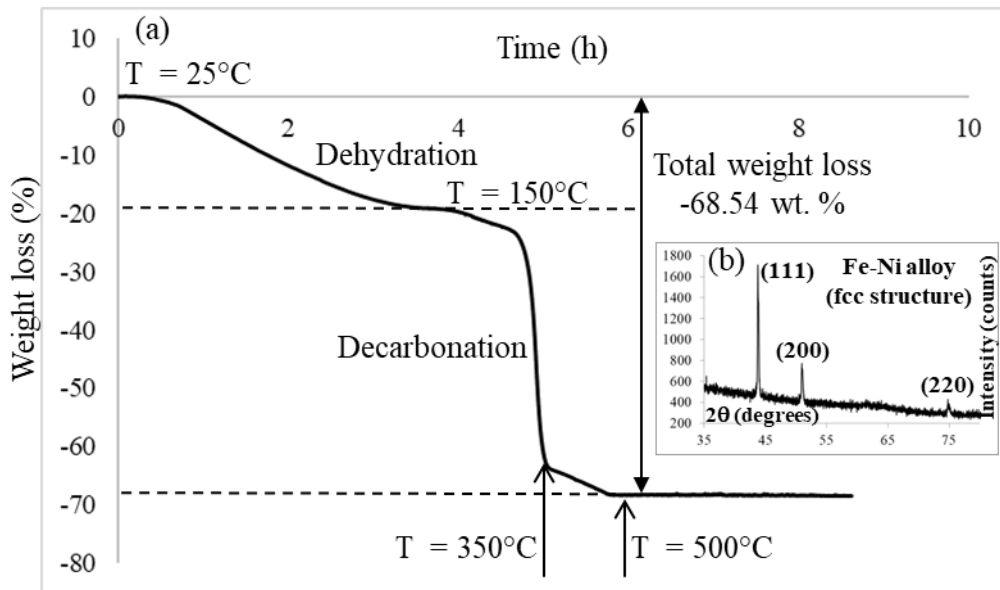


**Figure 2.** (a) Thermogram relating to thermal decomposition of the metal oxalate precursor ( $2.5^{\circ}\text{C} \cdot \text{min}^{-1}$  up to  $600^{\circ}\text{C}$ , dwell of 2 hours) and (b) X-ray diffraction pattern of the decomposition product.

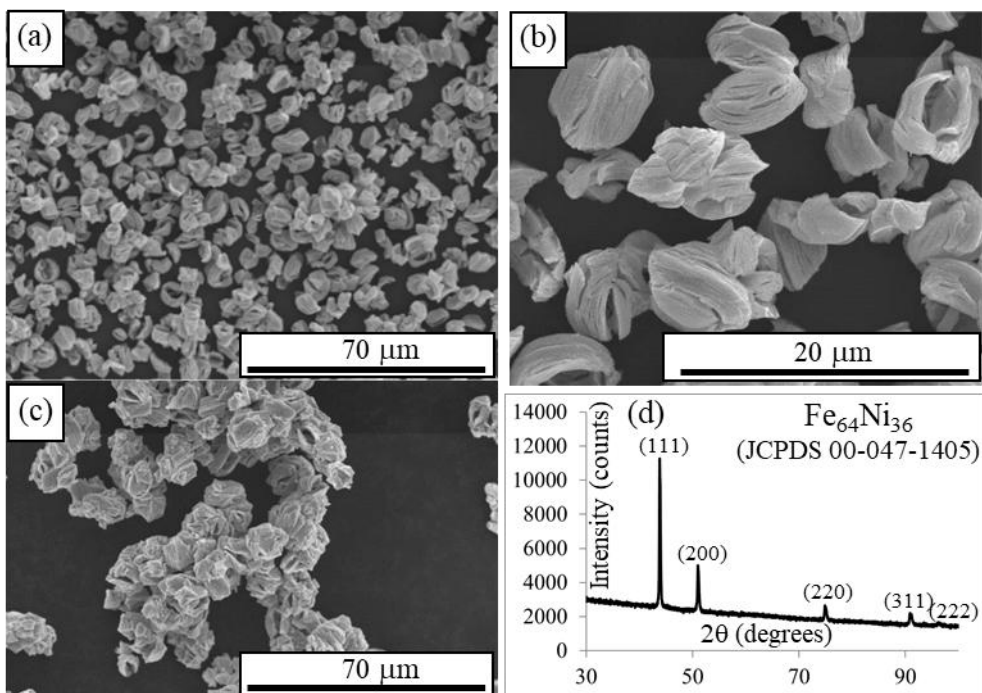


**Figure 3.** Fe<sub>64</sub>Ni<sub>36</sub> Invar alloy particles synthesized at the laboratory scale by thermal decomposition of the oxalate precursor at T temperature (a) and (b) SEM micrographs,

T = 550°C (c) SEM micrograph, T = 600°C, (d) X-ray diffraction pattern of the Invar powder obtained at 550°C.

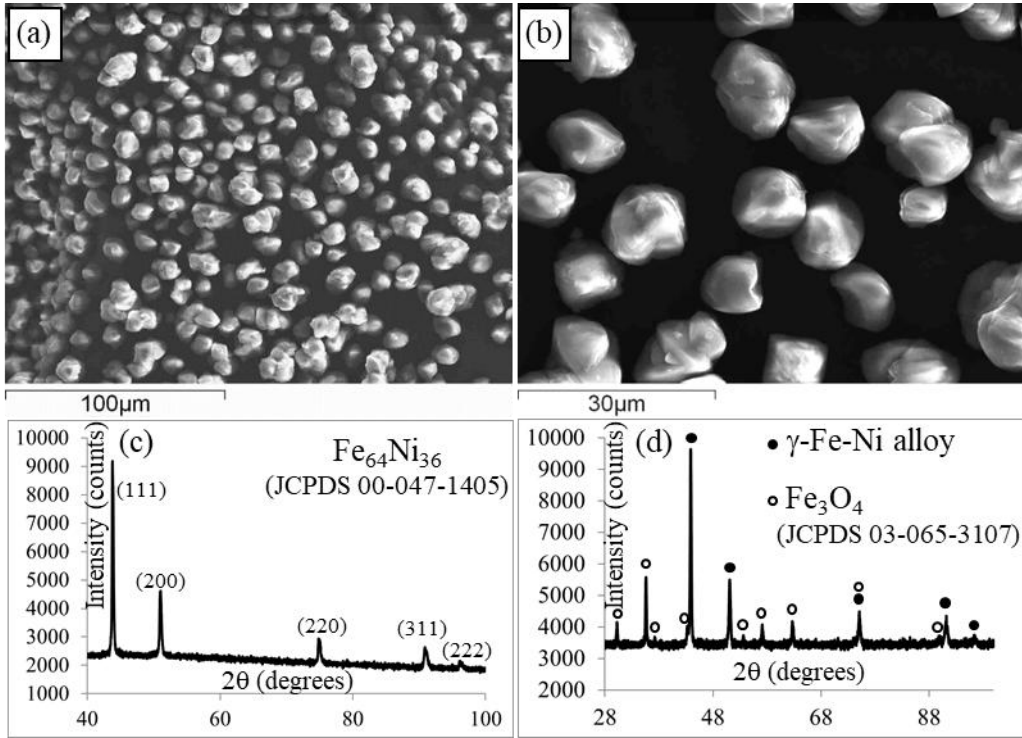


**Figure 4.** P oxalate precursor synthesized at the pilot scale (a) and (b) SEM micrographs (c) and (d) X-ray diffraction patterns of the P oxalate thermally decomposed at the laboratory and pilot scale, respectively.

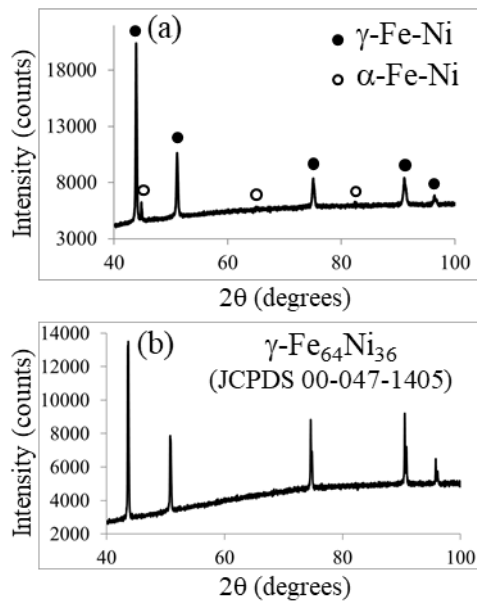


**Figure 5.** Thermal treatment carried out, under 3.9 vol. % H<sub>2</sub> in N<sub>2</sub>, on the Fe<sub>50</sub>Ni<sub>50</sub>-Fe<sub>3</sub>O<sub>4</sub> composite powder compacted at 250MPa (a) at 550°C, 10h and (b) followed by 1000°C, 2h.

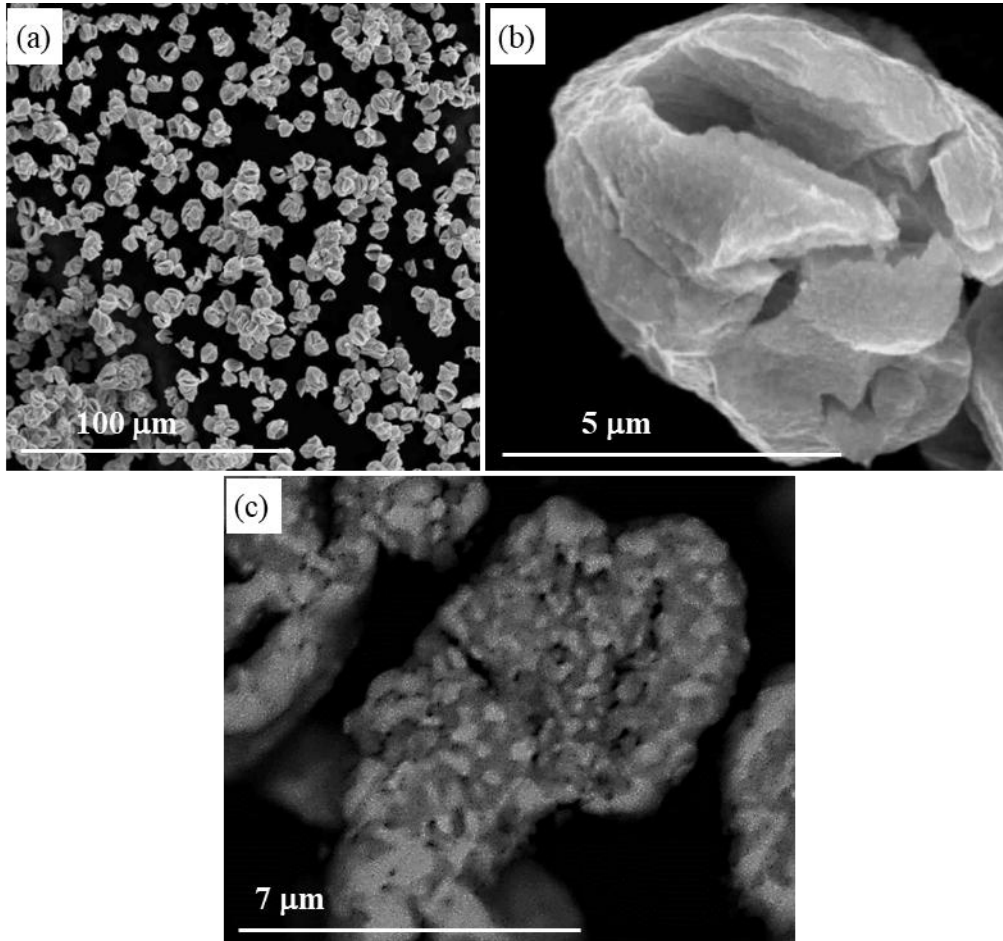


**Figure 6.** SEM micrographs of the Fe<sub>50</sub>Ni<sub>50</sub>-Fe<sub>3</sub>O<sub>4</sub> composite powder synthesized by thermal decomposition at the pilot scale of the P oxalate precursor (a) overview of the particles (b) particles opening and (c) composite powder microstructure.

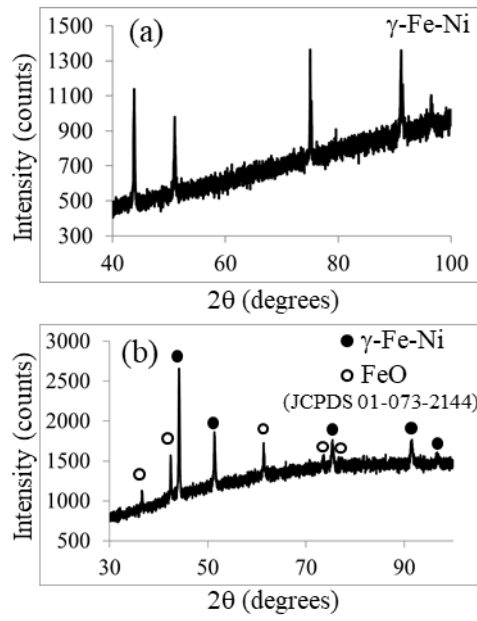


**Figure 7.** X-ray diffraction patterns of a laser processed sample with the parameters: power 45W, scanning speed 2000 mm. s<sup>-1</sup>, hatch spacing 5 μm (a) top surface and (b) bottom surface.

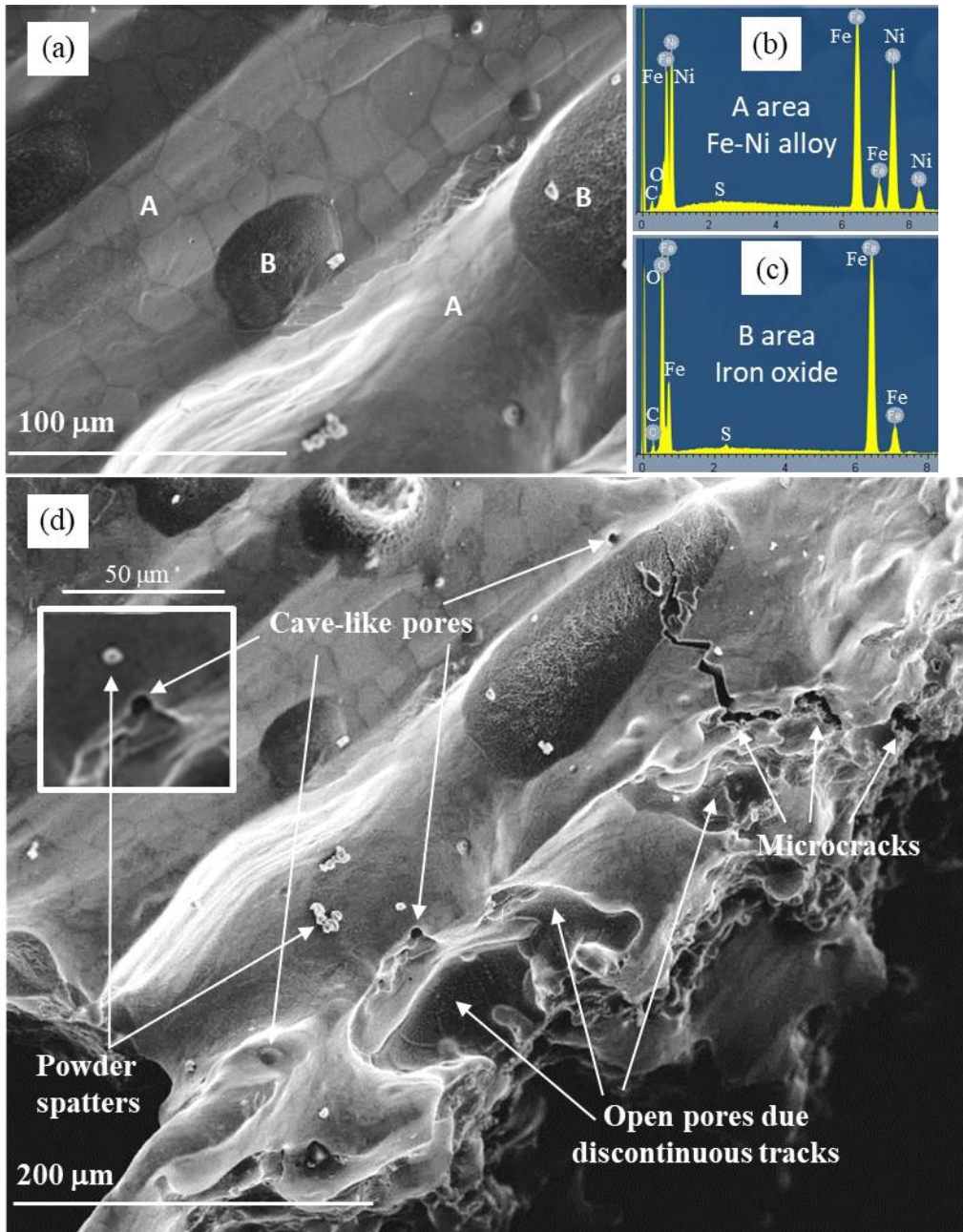


**Figure 8.** SEM observations of the top surface of a 45-2000-5 sample (a) and (d) SEM micrographs (b) and (c) EDX analyses. The presence of the Sulphur element is due to external contaminations.

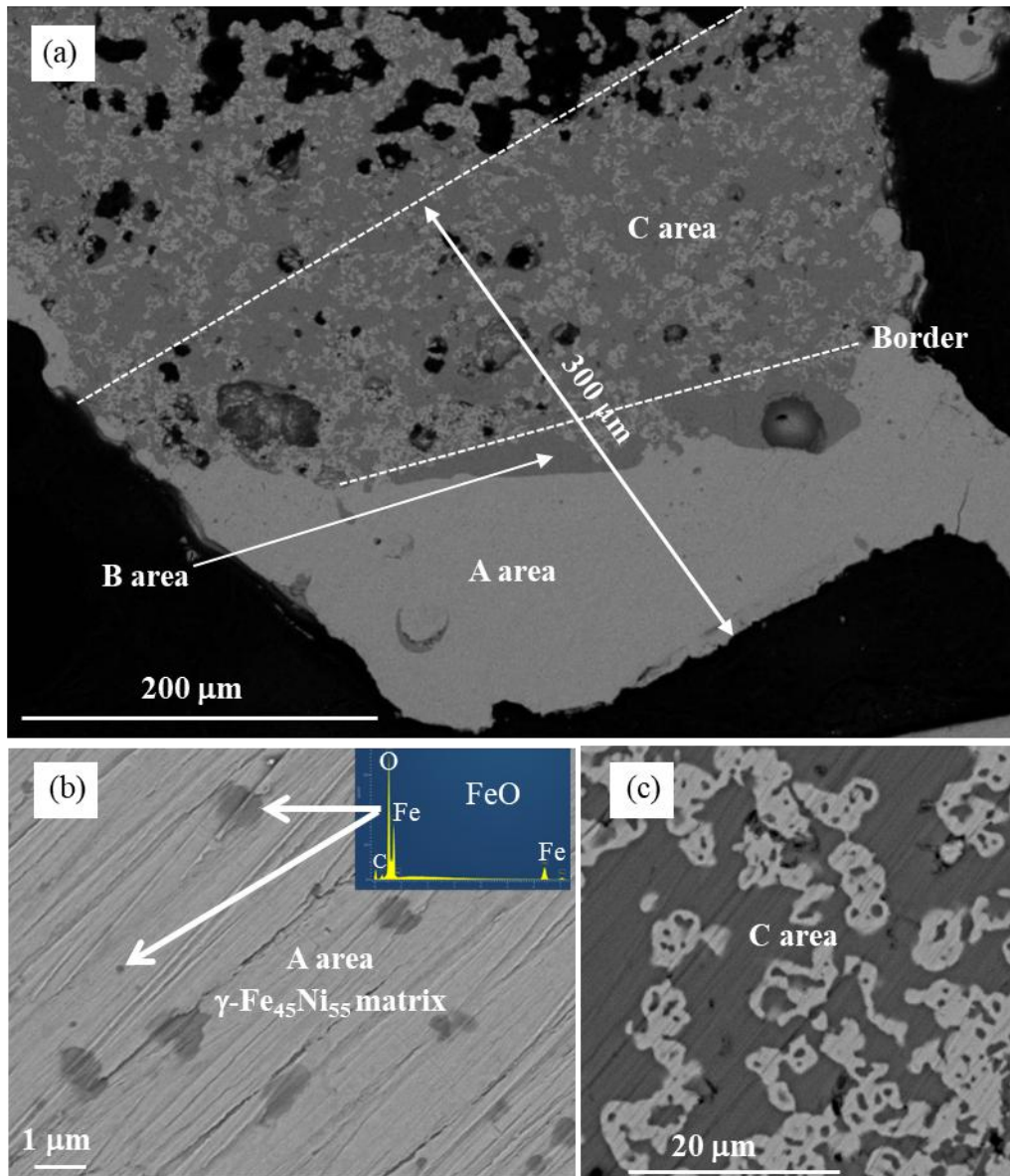


**Figure 9.** SEM observations of the side surface of a 45-2000-5 sample (a) overview of the side surface (b) dispersion of FeO particles into the  $\gamma$ -Fe<sub>45</sub>Ni<sub>55</sub> metallic area (c) microstructure of the  $\gamma$ -Fe<sub>47</sub>Ni<sub>53</sub>-FeO composite area.

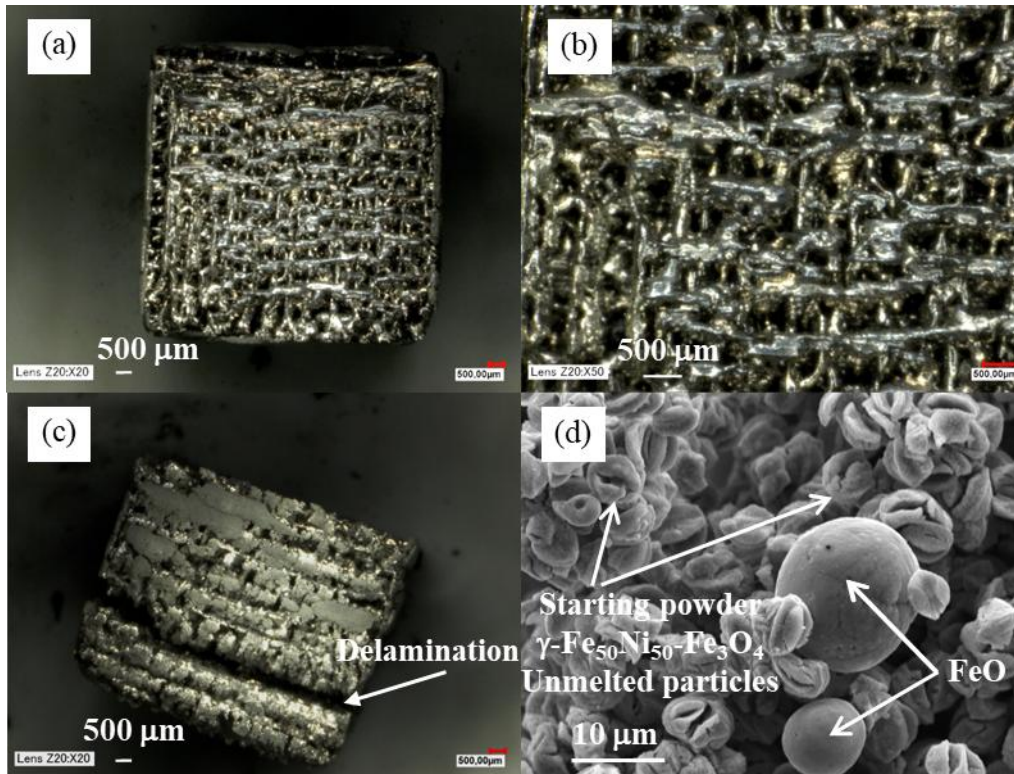


**Figure 10.** Optical micrographs of a 45-2000-5 3D part (a) and (b) top surface (c) side surface (d) SEM micrograph showing unmelted starting composite particles trapped between two adjacent powder beds.

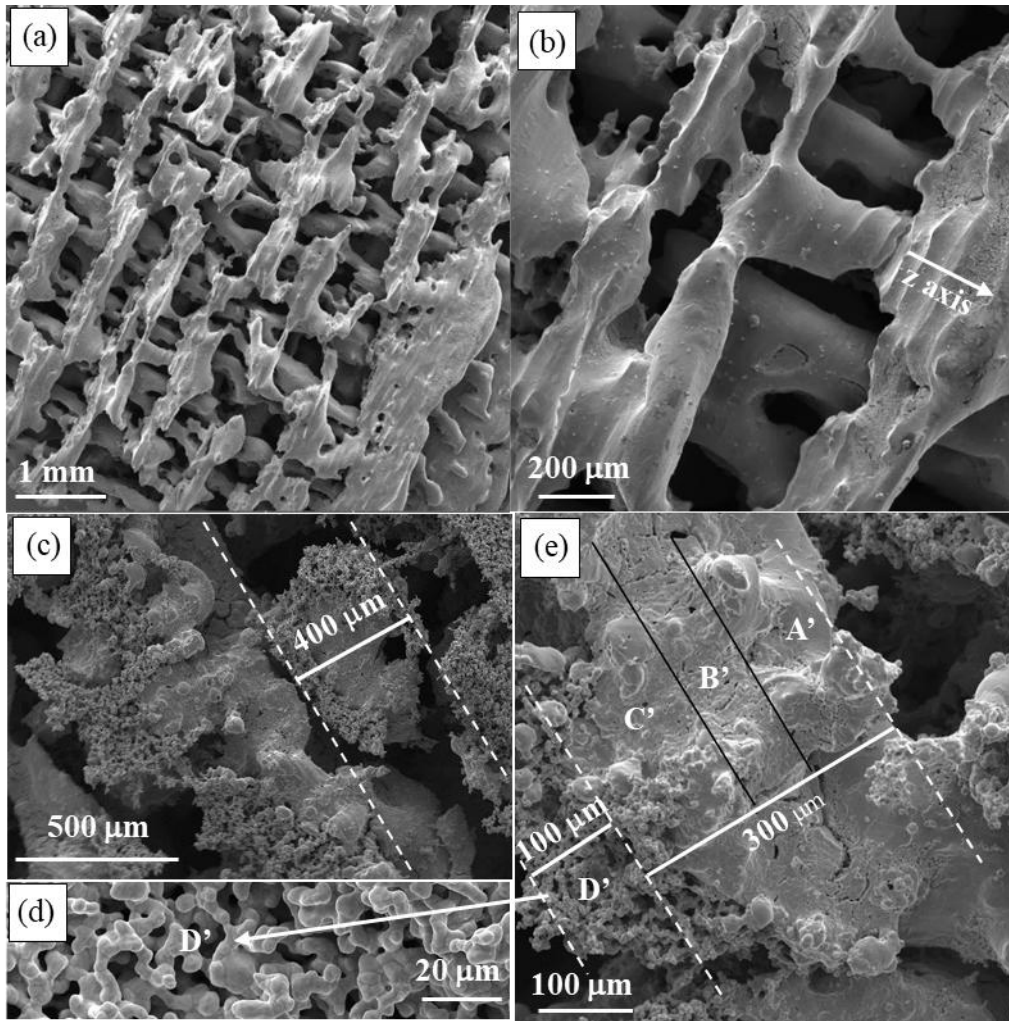


**Figure 11.** SEM micrographs of a 45-2000-5 3D part thermally post-treated under 3.9 vol. % H<sub>2</sub> in nitrogen (a) and (b) top surface (c), (d) and (e) side surface.

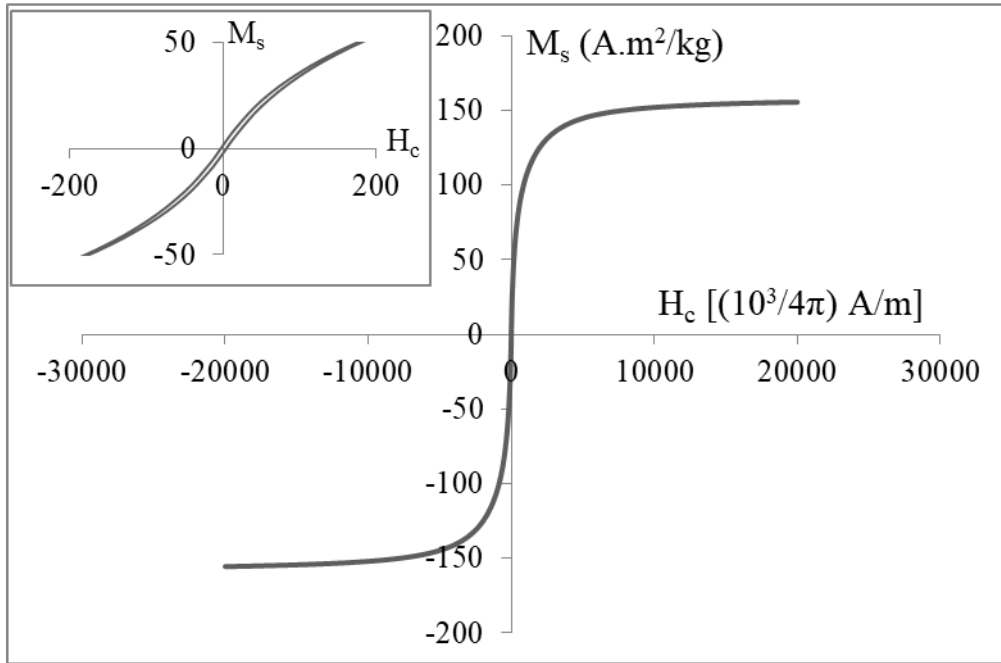


**Figure 12.** Magnetic hysteresis loop of a LPBF processed 45-2000-5 sample then conventionally heat treated (measurement at 300K).

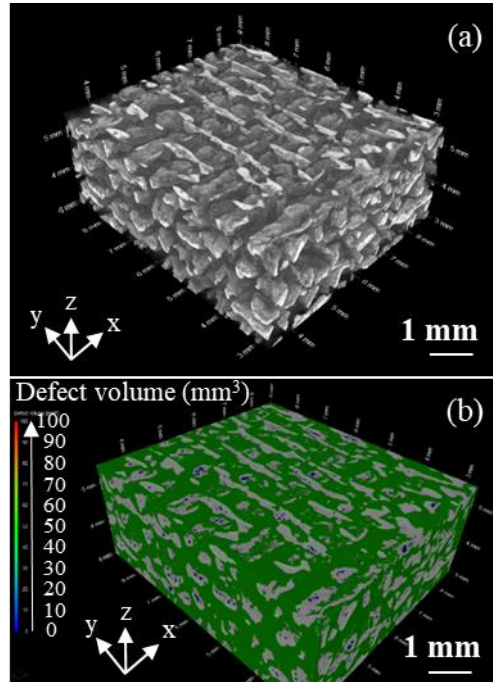


**Figure 13.** (a) and (b) X-ray micro-tomography micrographs of the central area of a LPBF processed 45-2000-5 3D part then conventionally heat t